

Intratumoral Biosynthesis of Gold Nanoclusters by Pancreatic Cancer to Overcome Delivery Barriers to Radiosensitization

Aaron S. Schwartz-Duval, Yuri Mackeyev, Iqbal Mahmud, Philip L. Lorenzi, Mihai Gagea, Sunil Krishnan,* and Konstantin V. Sokolov*



Cite This: *ACS Nano* 2024, 18, 1865–1881



Read Online

ACCESS |



Metrics & More



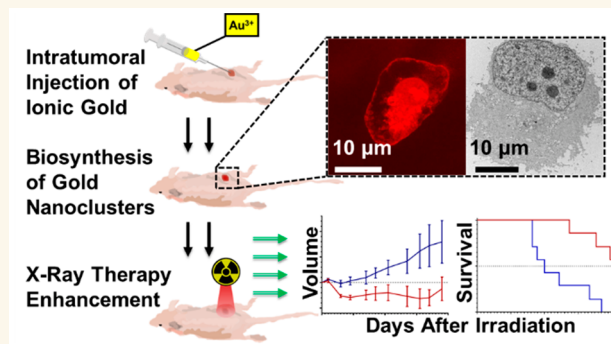
Article Recommendations



Supporting Information

ABSTRACT: Nanoparticle delivery to solid tumors is a prime challenge in nanomedicine. Here, we approach this challenge through the lens of biogeochemistry, the field that studies the flow of chemical elements within ecosystems as manipulated by living cellular organisms and their environments. We leverage biogeochemistry concepts related to gold cycling against pancreatic cancer, considering mammalian organisms as drivers for gold nanoparticle biosynthesis. Sequestration of gold nanoparticles within tumors has been demonstrated as an effective strategy to enhance radiotherapy; however, the desmoplasia of pancreatic cancer impedes nanoparticle delivery. Our strategy overcomes this barrier by applying an atomic-scale agent, ionic gold, for intratumoral gold nanoparticle biosynthesis. Our comprehensive studies showed the cancer-specific synthesis of gold nanoparticles from externally delivered gold ions *in vitro* and in a murine pancreatic cancer model *in vivo*; a substantial colocalization of gold nanoparticles (GNPs) with cancer cell nuclei *in vitro* and *in vivo*; a strong radiosensitization effect by the intracellularly synthesized GNPs; a uniform distribution of *in situ* synthesized GNPs throughout the tumor volume; a nearly 40-day total suppression of tumor growth in animal models of pancreatic cancer treated with a combination of gold ions and radiation that was also associated with a significantly higher median survival versus radiation alone (235 vs 102 days, respectively).

KEYWORDS: biomineralization, gold nanoparticles, *in situ* therapies, radiosensitization, pancreatic cancer



Localized therapies are a critical component of cancer treatment, and there is a renewed interest in innovative ways of intensifying radiotherapy for cancer treatment. The increased toxicity and lack of survival benefit from the elective irradiation of locoregional nodal basins has prompted a shift toward dose-escalation strategies that focus on just the primary tumor.¹ The initially reported role of dose escalation² was corroborated by a recent multicenter study showing that a 3-week course of dose-escalated hypofractionated radiotherapy significantly improved local control and overall survival.³ However, the utility of radiotherapy is limited by the resistance of some cancer cells to radiation. Thus, there is a critical need to develop methods that increase the radiation dose delivered to cancer cells. An emerging approach to enhancing the radiation dose delivered to tumors is to use high atomic number (high-Z) materials such as hafnium oxide⁴ or gold

nanoparticles (GNPs)^{5–13} to transiently increase the radiation-interaction probability of the target tissues. This effect is attributed to an increase in photoelectric absorption interactions due to the high Z of gold followed by the greater physical damage to tumor and endothelial cells caused by secondary (photo and Auger) electrons from nanoparticles.^{5–13}

Optimum enhancement of RT by GNPs or other high Z nanoparticles (NPs) requires: (1) efficient delivery to the

Received: May 12, 2023

Revised: December 22, 2023

Accepted: December 27, 2023

Published: January 11, 2024



tumor, (2) homogeneous uptake by the cancerous cells, and (3) intranuclear localization. The strategies for delivery of NPs to solid tumors were recently summarized in a comprehensive review by Izci et al.¹⁴ The inefficiency of delivery of NPs to solid tumors was highlighted by a meta-analysis, suggesting that only ~0.7% of the total intravenously injected dose accumulates in tumors in preclinical tumor models.¹⁵ A follow up study by the same group showed that the delivery efficiency in murine cancer models could be increased to 12% if the administered dose exceeds 1 trillion nanoparticles that was attributed to saturation of the ability of Kupffer cells to uptake NPs;¹⁶ however, the clinical translatability of this concept still needs to be evaluated. Most of nanoparticle delivery strategies to solid tumors rely on the enhanced permeability and retention (EPR) effect.¹⁷ Maximization of the EPR effect for delivery requires tailoring the nanoparticle size and surface coating to optimize the relationship between circulation and clearance, as well as preventing recognition and clearance by immune cells.^{14,18–20} However, translation of EPR-reliant approaches could be severely limited by both the intra- and interpatient heterogeneity of this effect in the tumors of human patients.²¹ Because of the heterogeneity of the EPR effect, many studies have explored strategies to modify the tumor vascularization including permeabilization, normalization, disruption, or promotion of vascularization to enhance treatment efficiency.²² However, a response to these *in situ* vascular modification strategies can be variable between patients, might be associated with additional side effects, and would require additional spatial and temporal control.²² To enhance the retention component of the EPR effect, many researchers have applied active targeting strategies reliant on ligand binding.^{23–25} However, a recent study indicated that only ~2% of targeted NPs interact with cancer cells at the tumor site.²⁶ This observation could be associated with nanoparticle uptake by other cells in the tumor microenvironment such as tumor associated macrophages and fibroblasts.^{27,28} Further, the tumor expression profiles are often highly heterogeneous. To mitigate this problem, some studies have explored combinations of multiple targeting ligands on the same nanoparticle;²⁹ however, this strategy complicates the NP's synthesis as the number of targeting antibodies needs to be controlled in order to maintain targeting efficiency.³⁰

Recent biomimetic strategies for nanoparticle delivery use extracted cell membrane or membrane derived extracellular vesicles (EVs).^{31–44} Membrane-coated NPs derived from blood cells were shown to significantly improve blood circulation time and even the ability to home to tumors via inflammation associated pathways.^{31–35,43} NPs coated with cancer-derived cell membranes “inherit” the cancer cells' ability to evade immune detection in combination with homotypic adhesion properties for tumor targeting.^{36–38} However, cell membrane coating strategies are complicated by difficulties in acquiring and storing the source material in high quantities.^{39–41} Similar to membrane coated NPs, EVs have shown considerable promise in immune escape and tumor targeting properties.^{45–47} However, the translation of EVs to clinical applications is currently limited by isolation procedures, which have low purity, low yield, and low loading capacity.⁴⁷

Moreover, in most cases, NPs are confined to cellular endosomal compartments following intracellular uptake that limits their radiosensitization potential.^{48,49} An additional challenge facing nanoparticle delivery, even for advanced targeted approaches, is that many solid tumors are

characterized with an exuberant interstitial matrix of glycosaminoglycans, collagen, and proteoglycans (i.e., desmoplasia) that serves as a physiological barrier to the delivery of even very small nanoparticles.^{14,50} Because the stroma also confines cancer cells to the tumor, depleting the stroma, and thus risking metastasis, may not be an effective strategy for improved nanoparticle delivery and radiation dose escalation.^{51,52}

To address these delivery challenges, we explored a radiosensitization strategy where ionic gold (Au^{3+}) is used as a precursor for the *in situ* biomineralization of GNPs and gold nanoclusters (GNCs) within the tumor. Changing the current paradigm from the delivery of premade GNPs, which are 5–200 nm, to the delivery of Au^{3+} , which are approximately 0.3 nm, is associated with an $\sim 4.6 \times 10^3$ to 3×10^8 reduction in volume of a gold therapeutic agent that is much more likely to uniformly diffuse throughout a desmoplastic tumor microenvironment. This strategy is founded on recent reports of mammalian cells' biomineralization of GNPs.^{53–66} These studies showed the colocalization of intracellularly formed nanoparticles within the cells' nuclei^{53–55,65} and indicated that GNP biomineralization from the application of chloroauric salts occurs more readily in cancer cells than in normal cells.^{56–59,61} They also provided evidence of intratumoral gold biomineralization in xenograft mouse models.^{56,58,65,67} In addition, injectable gold-salt solutions have been used safely for more than 80 years in the treatment of rheumatoid arthritis.⁶⁸ Furthermore, the prolonged use of injectable gold-salt drugs was found to lead to a mild side effect (i.e., chysiasis) due to in-patient GNP formation,^{69–71} thus providing additional proof of the feasibility of *in situ* gold biomineralization. However, *in situ* gold biomineralization has not been considered for applications in radiotherapy or thoroughly evaluated for other clinically translatable applications.

In the present study, we evaluated a gold biomineralization-based radiosensitization strategy in a model of pancreatic cancer, an aggressive malignancy whose yearly incidence nearly equals its mortality rate and the classic example of a recalcitrant, difficult-to-treat tumor.⁷² In the present study, we characterized cellular biosynthesis of GNCs, finding preferential Au^{3+} uptake and particle formation, with innate nuclear localization, by cancerous compared against normal cells. We then optimized the Au^{3+} treatment conditions to maximize particle formation with minimal impact to cell viability. The optimized treatment was used for mechanistic studies of ion internalization and cancer cell radiosensitization including DNA repair disruption, metabolic dysregulation, and lipid breakdown, which we further interrogated using combined lipidomic and metabolomic strategies. Finally, we quantified biodistribution, toxicity, and radiosensitization *in vivo* using a xenograft mouse model of pancreatic cancer, finding strong tumor colocalization of *in situ* formed GNPs, minimal treatment-related toxicity, and a strong radiosensitization effect.

RESULTS AND DISCUSSION

Intracellular Gold Reduction by Pancreatic Cells. For the initial investigation of pancreatic cancer cells' biomineralization of GNPs, we used common treatment parameters reported previously for other mammalian cells,⁷³ i.e., 1.0 mM chloroauric acid (as the source of Au^{3+} gold ions) in full cell media for 24 h. Live-cell confocal microscopy without staining (to eliminate the possibility of stain-induced Au^{3+} reduction)

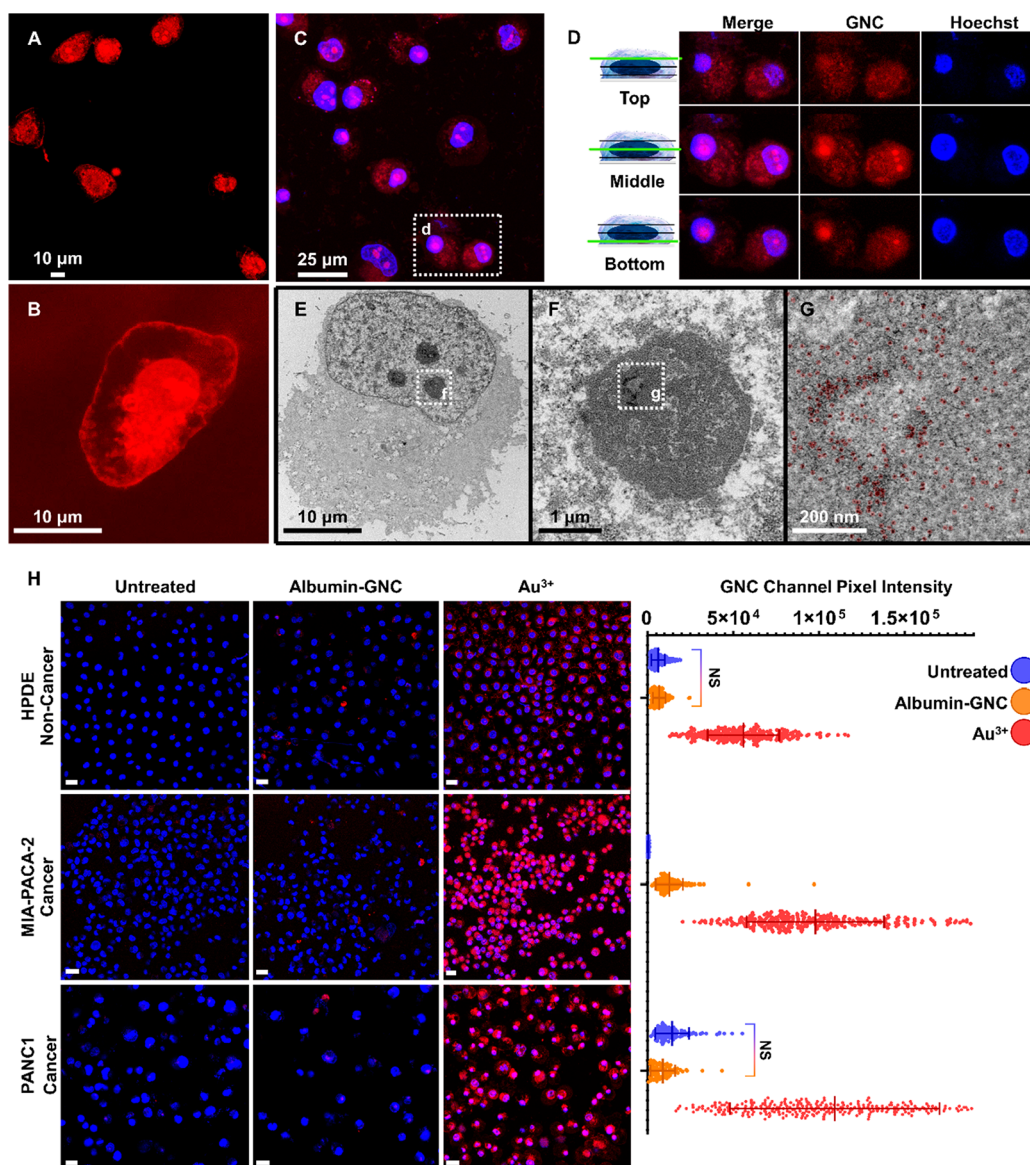


Figure 1. *In situ* GNP biomaterialization in pancreatic cancer cells. (A, B) Confocal fluorescence images of intracellularly formed GNCs ($\lambda_{\text{ex}}561/\lambda_{\text{em}}610$ nm) in live PANC1 cells after 24 h of treatment with 1.0 mM chloroauric acid without additional staining. (C, D) Maximum projection image (17 slices; C) and cross-sectional confocal images (D) of the top, middle, and bottom optical slices of live PANC1 cells showing intracellularly formed fluorescent GNCs (red) overlaid with Hoechst 33342 nuclear staining (blue) after 24 h of treatment with 1.0 mM chloroauric acid. (E–G) TEM images of PANC1 cells after 24 h of treatment with 1.0 mM chloroauric acid (E); magnified images of the nucleoli showing GNCs highlighted in red (F, G). (H) Confocal fluorescence images of the GNC signal (red) overlaid with Hoechst 33342 nuclear staining (blue) in live HPDE, Mia-PaCa-2, and PANC1 cells after 24 h of treatment with 1.0 mM gold as either prefabricated albumin-coated GNCs (Albumin-GNC) or chloroauric acid (Au^{3+}); untreated cells were the negative control. Scale bars are 25 μm . The quantification of relative GNC fluorescence is shown on the right; all differences were significant ($P < 0.0001$) except those marked “NS” (not significant; $P > 0.5$; ordinary 1-way ANOVA for multiple comparisons).

revealed a strong fluorescence signal characteristic of GNC formation^{56,58,59,61} in the Au^{3+} treated cells (Figure 1A,B) that was absent in the untreated cells (Figure S1). The fluorescence was detected in structures whose appearances were consistent with cellular and nuclear membranes, intracellular vesicles, and nuclei (Figure 1B). Emission spectra obtained with 561 nm laser excitation from different subcellular locations (i.e., cytoplasmic membrane, cytosol and nuclei) revealed peaks around 600–610 nm (Figure S1b,c) with the fluorescence intensity from GNCs in the nucleoli ~ 125 -fold greater than the cytosolic or membrane fluorescence (Figure S1b,c). Subsequent cross-sectional confocal imaging with Hoechst

33342 nuclear staining and transmission electron microscopy (TEM) confirmed the intranuclear localization of GNCs in the treated cells (Figure 1C–G). The intranuclear fluorescence from GNCs exhibited a pattern with bright loci that was consistent with nucleoli. TEM images showed consistently higher mean electron density values for the nucleoli of treated PANC1 cells, with identifiable GNCs with a mean size of 3.1 ± 1.8 nm ($n = 2196$ particles) (Figure S2a–f).

Next, we compared the cellular biomaterialization of GNCs with uptake of prefabricated albumin-coated GNCs (Figure S2g,h) in two pancreatic cancer cell lines (PANC1 and Mia-PaCa-2)⁷⁴ and in noncancerous human pancreatic duct

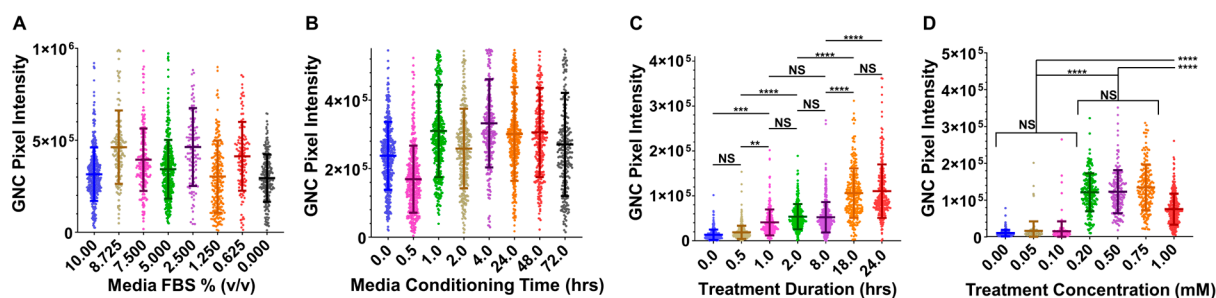


Figure 2. Optimization of *in situ* GNP biomineralization. (A–D) Quantification of total intranuclear GNC channel pixel intensity per cell, measured from confocal fluorescence images ($n = 3$ images) of live PANC1 cells after treatment with chloroauric acid in cell media with various FBS concentrations (% v/v; A), media conditioning times (B), chloroauric acid treatment durations (C), or chloroauric acid treatment concentrations (D). Standard treatment conditions were 10% (v/v) FBS; 24 h of media conditioning by cells before treatment with chloroauric acid; 24 h of treatment with chloroauric acid; treatment with 1.0 mM chloroauric acid. Representative confocal images of the cells used in these analyses are provided in Figure S3. Error bars are standard deviations. ^{NS} $P > 0.05$, ^{*} $P < 0.05$, ^{**} $P < 0.01$, ^{***} $P < 0.001$, and ^{****} $P < 0.0001$; ordinary 1-way ANOVA for multiple comparisons.

epithelial (HPDE) cells. Confocal fluorescent imaging confirmed that both cancer cell lines had GNC biomineralization, which occurred with approximately 2-fold greater efficiency than in the noncancer cells ($P < 0.0001$ for both comparisons) (Figure 1H). Compared with prefabricated albumin-coated GNCs, Au³⁺ treatments resulted in 12- and 7-fold greater fluorescence in PANC1 and Mia-PaCa-2 cells, respectively (Figure 1H). These findings indicate that the albumin in the cell culture media does not enable extracellular biomineralization with subsequent uptake of extracellularly formed GNCs in Au³⁺-treated cells. Indeed, if the extracellular albumins were responsible for reducing gold ions, then the cells treated with prefabricated albumin-coated GNCs would have had a fluorescence signal comparable to that from the cells treated with gold ions. Further confirming this conclusion, we found that supplementing the incubating cell media with various amounts of fetal bovine serum (FBS) before treatment with Au³⁺ was not associated with any consistent trend in GNC fluorescence from biomineralization (Figures 2A and S3a).

Optimization of Treatment Conditions for Intracellular GNC Biomineralization. We investigated how cell secretions, the Au³⁺ treatment duration, and the Au³⁺ concentration influence the fluorescence signal from GNCs formed inside PANC1 cells (Figure 2B–D, Supporting Information, and Figure S3b–d) and then interrogated how those variables influence cellular viability (Figure S4f–i). Media preconditioning with PANC1 cells up to 72 h did not reveal any identifiable trends in intranuclear fluorescence of GNCs (Figure 2B). The fluorescence signal steadily increased after 1 h of incubation with Au³⁺ ions achieving the maximum value of ~ 18 h (Figure 2C). Concentrations of 0.20–0.75 mM Au³⁺ resulted in the greatest fluorescence intensity (Figure 2D) while Au³⁺ treatments with ≤ 0.20 mM did not significantly impact PANC1 cell viability (Figure S4f–i). Based on these optimization studies, the following conditions for Au³⁺ treatment in cell culture were used for subsequent studies unless otherwise stated: 24 h incubation of cells in media with 10% (v/v) FBS followed by 0.20 mM Au³⁺ treatment for 24 h.

Interrogation of Gold Ion Uptake. The specific mechanisms of gold ion entry in mammalian cells are not fully understood. However, prior studies indicate that Au³⁺ uptake occurs through mechanisms distinct from classical nanoparticle pathways and that pathways for Au³⁺ uptake are more efficient than the classical pathways, which are common

for prefabricated nanoparticles.^{60,65} Schwartz-Duval et al.⁶⁵ used a combination of molecular inhibitors and genomic studies to demonstrate that the classical nanoparticle uptake pathways (i.e., energy-dependent-, dynamin-dependent-, lipid raft-, clathrin-dependent-, and clathrin-independent-based uptakes) were not involved in the uptake of gold ions. Additionally, these studies showed no significant difference in gold uptake between cells with inhibited endocytosis pathways and controls that suggests a negligible uptake of extracellularly formed nanoparticles, which commonly occurs through various endocytosis mechanisms.⁶⁵ The latter result was supported by Drescher et al.⁶⁰ who directly compared the uptake of gold ions with prefabricated particles and observed a much greater cellular uptake of gold ions. Our data in Figure 1H are in a good agreement with these reports as we observed a negligible uptake of prefabricated GNCs compared to *in situ* biomineralization of GNCs by pancreatic cells. We also determined that neither serum albumins nor secreted biomolecules are majorly involved in shuttling Au³⁺ inside cells as there were no clear dependence of GNC intracellular formation on either concentration of FBS or media conditioning time, respectively (Figure 2A,B).

Therefore, we decided to explore the feasibility of involvement of cellular ion channels in the uptake of gold ions. To test this hypothesis, we coapplied titrated dosages of physiologically relevant cations with atomic radii comparable to Au³⁺ (i.e., Mg²⁺, Ca²⁺, Mn²⁺, Fe³⁺, and Fe²⁺) at high and medium Au³⁺ concentrations (i.e., 1.0 and 0.5 mM, respectively). GNC fluorescence was used to assay *in situ* gold biomineralization. Among the selected cations, magnesium has the greatest intracellular abundance (10–30 mM)⁷⁵ while the other cations (i.e., Ca²⁺, Mn²⁺, Fe³⁺, and Fe²⁺) are present at lower concentrations. The physiological cation concentrations were used to set the titration doses.

We observed that cotreatments with Mg²⁺ and Ca²⁺ ions (Figure 3A,B, respectively) resulted in a linear increase in GNC fluorescence at 1.0 mM Au³⁺ while there was no correlation at 0.5 mM Au³⁺. A prior study by Zhao et al.⁵⁸ showed that biomineralization of GNCs from Au³⁺ could be enhanced by increasing intracellular ROS formation that was induced by the addition of Fe²⁺ ions. Therefore, we evaluated ROS formation and metabolic cell viability at Mg²⁺ and Ca²⁺ concentrations used in our study and found no substantial changes in either parameter that excludes the possibility of ROS involvement in the observed increase in GNC

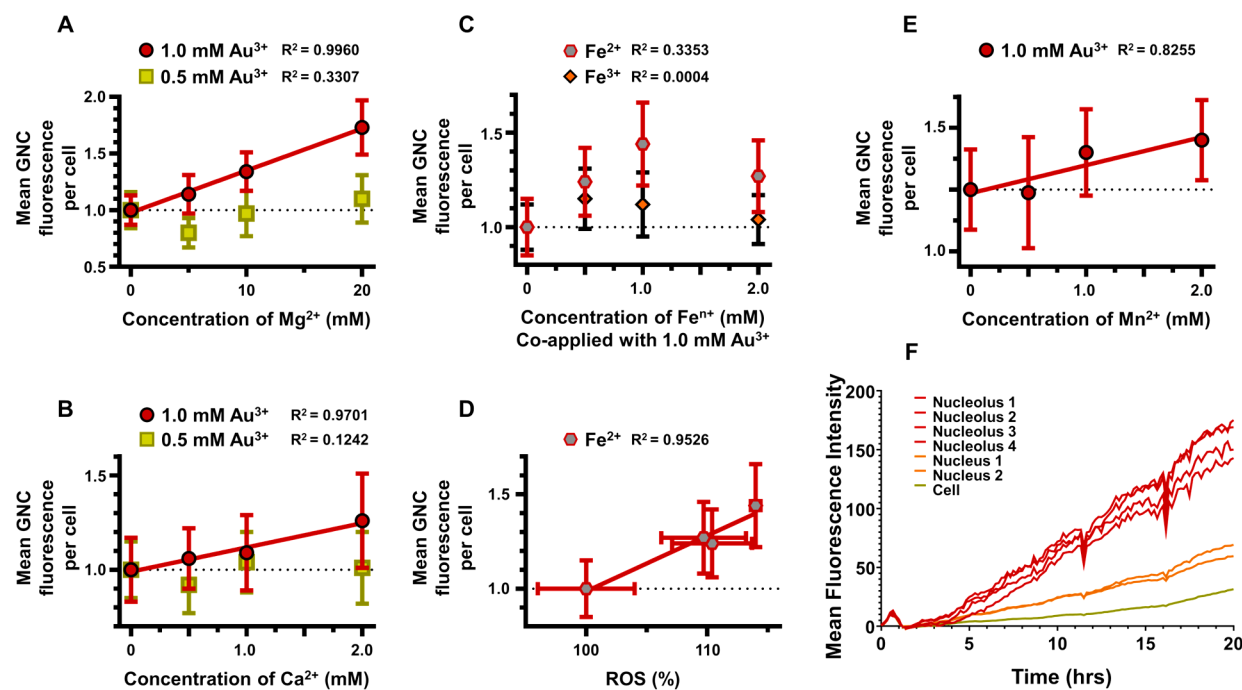


Figure 3. Interrogation of gold ion uptake for *in situ* GNC biomineralization. (A–E) Plots showing relationships between mean GNC fluorescence from Au^{3+} biomineralization and coapplications of physiological cations Mg^{2+} (A), Ca^{2+} (B), Fe^{2+} and Fe^{3+} (C), ROS formation from Fe^{2+} treatment (D) and Mn^{2+} (E) over a 24 h period at varied physiologically relevant cation concentrations in PANC1 cells. (F) Mean fluorescence intensity measurements collected once every 10 min for 20 h for specific regions of interest, such as the cellular nucleolus, nucleus, and whole cell, during treatment of PANC1 cells with 0.20 mM chloroauric acid in full cell media under normal incubation conditions. Fluorescence data points and error bars (standard deviations, $n = 3$) are from confocal microscopy images.

biomineralization (Figure S5a–d). In addition, we showed that cell cotreatment with Fe^{2+} ions results in an increase in GNC fluorescence (Figure 3C) and Fe^{2+} treatment induces ROS production (Figures 3D and S5e,f), which is in agreement with the study by Zhao et al.⁵⁸ Cell cotreatment with Fe^{3+} showed no correlation with GNC fluorescence (Figure 3C), and there was no substantial effect of Fe^{3+} treatment on either cell viability or ROS production (Figure S5g,h). We also found a linear correlation between Mn^{2+} supplement and GNC fluorescence (Figure 3E); however, this correlation may be influenced by the impact Mn^{2+} had on cellular viability rather than ROS induction (Figure S5i,j).

Data in Figure 2D indicate that GNC fluorescence decreases when the concentration of Au^{3+} is increased to 1.0 mM. Therefore, the positive correlation between the concentration of Mg^{2+} and Ca^{2+} ions and GNC fluorescence at 1.0 mM Au^{3+} might indicate a competition for cellular entry pathways that effectively decreases gold ion uptake resulting in an increase of GNC fluorescence. The lack of correlation between cotreating cations and the GNC fluorescence at 0.5 mM could be due to the plateau in GNC fluorescence between 0.2 and 0.75 mM Au^{3+} , suggesting that a decrease in effective Au^{3+} concentration below 0.5 mM, but above 0.2 mM, would not be associated with a GNC fluorescence change (Figure 2D). Therefore, our cation cotreatment study suggests that Mg^{2+} and Ca^{2+} ions and their channels as interesting candidates for future exploration of Au^{3+} cell uptake and *in situ* gold biomineralization in general.

The total gold content, measured by ICP-MS under optimized conditions, showed Mia-PaCa-2, PANC1, and HPDE cells had uptakes of the total gold dose of $18.3 \pm 2.1\%$, $19.0 \pm 3.6\%$, and $13.7 \pm 1.2\%$, respectively (Figure S6a),

linearly correlated ($r^2 = 0.57$, $P = 0.0185$) with the intranuclear GNC fluorescence shown in Figure 1H (Figure S6b). Interestingly, the difference in intracellular synthesis of GNCs between the cancerous and noncancerous cells as assessed by fluorescence is significantly more pronounced than the difference between the total gold uptake from ICP-MS.

Next, we evaluated the locoregional time dependence of *in situ* biomineralization of GNCs and the potential intracellular trafficking of the formed GNCs into nuclei using longitudinal live cell imaging, as well as characterized the labeling efficiency at the 24 h time point under optimized treatment conditions. For longitudinal live cell imaging, we transfected PANC1 cells with a Bacman Cell light nuclear GFP kit for initial localization of nuclei in confocal fluorescent live cell imaging. Then, we carried out the real-time visualization of the cellular biomineralization process (Supplementary Video 1). GNC fluorescence emerged simultaneously in the nucleus, nucleolus, nuclear membrane, cytosol, and cell membrane of all cells uniformly without any detectable fluorescence in the extracellular space. The overall fluorescence pattern did not change over time and had the same appearance as in the final images shown in Figure 1A–D. The fluorescence intensity steadily increased at different rates throughout the cell, with the highest and lowest rates observed in the nucleoli and cytosol, respectively (Figure 2F). These findings indicate that, within the time period explored, gold ions are able to permeate the cell unencumbered and without any transportation or trafficking of intracellularly formed GNCs. They also suggest that fluorescent GNC biomineralization occurs primarily through interactions within the cell and not through interactions with extracellular cell secretions. However, it is conceivable that some nonfluorescent GNPs could have

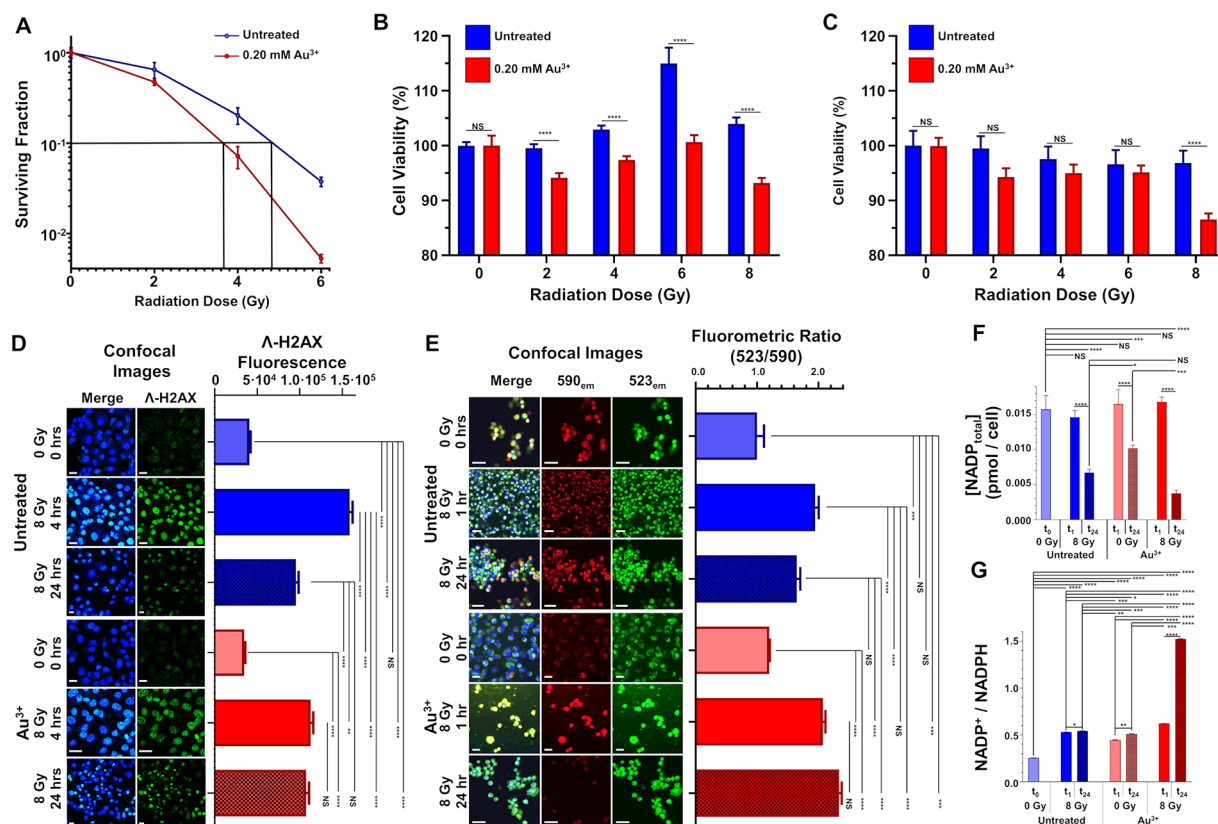


Figure 4. Radiosensitizing effects of GNCs biomaterialized *in situ*. (A) A clonogenic assay of PANC1 cells treated with or without 0.20 mM Au^{3+} and exposed to 0–6 Gy of X-ray radiation. The black lines intersecting the x -axis represent the radiation dose necessary to reduce the surviving fraction to 10%. (B, C) MTS of PANC1 cells treated with or without 0.20 mM Au^{3+} and exposed to 0–8 Gy of X-ray radiation at 24 h after irradiation (B) and 96 h after irradiation (C). (D) Confocal fluorescence images of double-stranded DNA breaks detected with fluorescent γ -H2AX antibody staining (green) overlaid with Hoechst 33342 nuclear staining (blue) in fixed PANC1 cells after treatment with Au^{3+} (0.00 or 0.20 mM) and X-ray radiation (0 or 8 Gy) at 0, 4, and 24 h after irradiation. The quantification of γ -H2AX fluorescence is shown on the right. (E) Confocal fluorescence images of relative mitochondrial polarization detected using fluorescent JC-1 staining (590 emission, red; and 523 emission, green) overlaid with Hoechst 33342 nuclear staining (blue) in live PANC1 cells treated with Au^{3+} (0.00 or 0.20 mM) and radiation (0 or 8 Gy) at 0, 1, or 24 h after irradiation. The quantification of the JC-1 fluorometric ratio (590/523) is shown on the right. The scale bars in (D) and (E) are 25 μm . (F, G) Total NADP (F) and $\text{NADP}^+/\text{NADPH}$ ratios (G) of PANC1 cells after treatment with Au^{3+} (0.00 or 0.20 mM) and radiation (0 or 8 Gy) at 0, 1, or 24 h after irradiation. Error bars are standard deviations. $^{\text{NS}}P > 0.05$, $^*P < 0.05$, $^{**}P < 0.01$, $^{***}P < 0.001$, and $^{****}P < 0.0001$; ordinary 1-way ANOVA for multiple comparisons.

formed within the extracellular space and were not detected by fluorescence imaging.

Flow cytometry showed $\sim 68\%$ PANC1 cells with a positive signal from GNCs following a 24 h treatment with 0.20 mM Au^{3+} in full cell media (Figure S6c). This result does not appear to fully correlate with our confocal fluorescence imaging where we observed the near uniform biosynthesis of GNCs by confocal imaging shown in Figures 1 and S3 and Supplementary Video 1. This discrepancy could be related to heterogeneity in biosynthesis of GNCs inside cells with ~ 7 -fold greater fluorescence from nucleoli relative to the entire cell (Figures 3F and S1). Therefore, a strong localized increase in nucleoli fluorescence is very prominent in confocal fluorescence microscopy, but in some cells, it might not result in an appreciable increase in the overall cell fluorescence that is detected by flow cytometry.

Radiosensitization of Pancreatic Cancer Cells by GNCs Synthesized *In Situ*. We used a standard clonogenic assay to evaluate the radiosensitization efficacy of intracellularly synthesized GNCs in PANC1 cells using the optimized treatment parameters described above (Figure 4A). At radiation doses of 2, 4, and 6 Gy, the mean surviving

fractions of PANC1 cells treated with Au^{3+} (47.3%, 7.2%, and 0.5%, respectively) were significantly lower than those of untreated control cells (64.9%, 20.3%, and 3.8%, respectively; $P < 0.0005$), and the dose enhancement factor at a surviving fraction of 10% was 1.317, indicating a strong radiosensitization in Au^{3+} -treated cells. In addition, we used an MTS assay to assess the short-term (i.e., 24 and 96 h) effects of radiosensitization on cell viability (Figure 4B,C). At 24 h, we noted that cells treated with 4, 6, or 8 Gy of radiation alone had increased viability, possibly due to radiation-stimulated proliferation,^{76–78} which is not necessarily reflected in a colony-counting clonogenic assay.⁷⁶ However, all Au^{3+} -treated cells had significantly decreased viability compared with their radiation only treated counterparts (Figure 4B). At 96 h, all groups except the Au^{3+} -treated cells irradiated with 8 Gy had returned to baseline viability (Figure 4C). Together, these findings indicate that 8 Gy of radiation combined with Au^{3+} induces significant short-term radiosensitization-based inhibition of cell viability and proliferation.

To characterize the mechanisms of radiosensitization, we first assessed the formation of double-strand DNA breaks using a γ -H2AX antibody assay.⁷⁹ Four hours after irradiation, Au^{3+} -

treated cells had 29% fewer DNA breaks than untreated cells (Figure 4D). After 24 h, however, the untreated cells had a significant recovery of DNA breaks (i.e., they had ~32% fewer breaks at 24 h than at 4 h; $P < 0.0001$) compared with the treated cells, which did not have a recovery of DNA breaks between 4 and 24 h ($P = 0.72$) (Figure 4D). Next, we used a tetraethylbenzimidazolylcarbocyanine iodide (JC-1) assay to assess mitochondrial depolarization, an early stage marker of apoptosis,^{80,81} and found no significant difference between the Au³⁺-treated and untreated cells 1 h after irradiation with 8 Gy. Compared with the nonirradiated cells, the irradiated cells had an approximately 2-fold-greater green/red fluorescence intensity ratio, indicating their increased mitochondrial depolarization (Figure 4E). Twenty-four hours after irradiation, the fluorescence intensity ratio of the untreated cells had decreased to 1.65 ± 0.06 , indicating a partial recovery of mitochondrial polarization, whereas that of the Au³⁺-treated cells had increased to 2.34 ± 0.04 (Figure 4E).

We also quantified changes in the total NADP (i.e., NADP⁺ and NADPH) and the NADP⁺/NADPH ratio to assess intracellular energy metabolism and redox potentials, respectively.⁸² Total NADP did not differ significantly between the Au³⁺-treated and untreated control cells 1 h after irradiation (Figure 4F). After 24 h, however, the levels of total NADP in the radiation-only, Au³⁺-only, and combination treatment groups were 57%, 35%, and 76% lower, respectively, than that in the untreated control group (Figure 4F). Most dramatically, the NADP⁺/NADPH ratio in the combination treatment group 24 h after irradiation was 2.8 times larger than that in the radiation-only group and 3.0 times larger than that in the Au³⁺-only group, indicating a severe metabolic deficit (Figure 4G). Interestingly, the NADP⁺/NADPH ratios of the cells receiving only radiation or Au³⁺ were approximately 2-fold higher than that of the untreated control cells, which suggests that Au³⁺ treatment has an adverse effect on the metabolism of pancreatic cancer cells.

Finally, a thiobarbituric acid reactive substance (TBARS) assay revealed an approximately 2-fold higher level of radiation-induced peroxidation products in cells treated with the combination of Au³⁺ and radiation versus those treated with radiation alone; cells treated with Au³⁺ alone showed no induction of peroxidation product formation (Figure S7a).

Together, these findings suggest that *in situ* gold biomineralization can cause a significant radiosensitization of pancreatic cancer cells that is predominantly associated with the disruption of DNA repair, dysregulation of metabolism, and breakdown of lipids. Despite the high level of intranuclear fluorescence due to GNC formation (as shown in Figure 1D), we found no evidence of increased DNA damage due to double strand break formation.

Metabolomic and Lipidomic Interrogation of Molecular Mechanisms of Radiosensitization by *in Situ* GNC Biomineralization. The specific mechanisms of the metabolic conversion of Au³⁺ to Au⁰ are not well established; however, a number of previous studies indicated the involvement of ROS/RNS,^{53,56–59,61} NADH dehydrogenase flavoprotein 2 and quinone oxidoreductase-like protein,⁵⁷ and glutamate,⁵⁹ as well as several proteins that bind cations, energetic metabolites, or nucleotides.^{62,65,83} If the formation of GNPs from gold ions were to disrupt the relative abundance of those biomolecules, this could enhance radiosensitization, complementing the sensitization afforded by the intracellular biosynthesis of gold particles. To explore the hypothesis that GNC biomineraliza-

tion could enhance radiosensitization by modulating cancer cell metabolism and also to uncover potential biological mechanisms of gold biomineralization, we treated PANC1 cells with Au³⁺ without radiation using untreated cells as a control and performed global metabolomic and lipidomic profiling using ultrahigh resolution liquid chromatography coupled to ultrahigh resolution mass spectrometry (UHPLC-HRMS). Au³⁺-treated cells had a metabolite profile distinct from untreated cells (Figure 5B). Differential analysis revealed that Au³⁺ treatment significantly perturbed redox metabolism including NADH metabolism, glutathione metabolism, and the tricarboxylic acid (TCA) cycle (Figure 5A,B). The connection between these changes in metabolite abundance and cellular gold biomineralization were reported in the literature. Redox metabolism such as ROS/RNS, glutamate, and NADH were directly indicated as involved in cellular biomineralization.^{53,56–59,61} Additionally, many of these metabolites were shown to reduce gold ions directly through benchtop synthesis (NADH, glutathione, and citrate).^{84–86}

Furthermore, Au³⁺ treatment significantly reduced fatty acid metabolism (Figures 5C and S7c) and nucleotide metabolism (Figures 5D and S7d). We also observed differential modulation of the central carbon network including glycolysis and pentose phosphate pathways (Figure S7e). The central carbon metabolic network such as the TCA cycle, NADH, and the pentose phosphate pathway (PPP) are intricately related to oxidative stress.⁸⁷ Together, we observed distinct perturbation in central carbon metabolism that may be associated with an imbalance of cellular redox status in Au³⁺-treated cells. Additionally, through lipidomics, we observed that Au³⁺ treatment modulated the global lipid profile of PANC1 cells (Figure S7f). Lipid ontology analysis revealed significant reduction of cardiolipins (CLs) (Figures 5E and S7g). Since CLs are associated with protein complexes of the mitochondrial electron transport system (ETS), reduction of CL levels can lead to instability and impaired function of ETS and potentially result in electron leakage and impaired mitochondrial bioenergetics and increase production of ROS.⁸⁸ This observed perturbation of CL prompts the hypothesis that the anticancer mechanism of GNC biomineralization could involve positive modulation of mitochondrial ROS production. Strikingly, Au³⁺ treatment decreased lipids known to be associated with signaling pathways for cell proliferation including diacylglycerol (DG) (Figures 5F and S7h), phosphatidylserine (PS) (Figures 5G and S7i), and phosphatidylinositol (PI) (Figures 5H and S7j).⁸⁹ Overall, these findings identify potential mechanisms underlying gold biomineralization in mammalian cells as well as GNC-mediated radiosensitization, with effects on oxidative stress and disruption of the cell cycle highlighted as recurring themes (Figure 5I).

Toxicity Assessment and Biodistribution. Toxicity was assessed in mice with PANC1 tumor xenografts 48 h after intratumoral injection of Au³⁺ in 20 μ L of PBS. Histopathological evaluation revealed similar systemic immune stimulation in all groups of mice: mice with Au³⁺ treated tumor and mice with sham (PBS) treated tumor (Table S1). Both groups had comparable lesions of lymphocytic hyperplasia, plasmacytosis, and histiocytosis of major lymphoid tissues, mesenteric lymph nodes, and spleen. In addition, all mice from both groups had moderate to marked lymphohistiocytic inflammation in the subcutaneous tissue around the tumor. It was noticed that one of the 4 mice from Au³⁺ tumor-treated mice

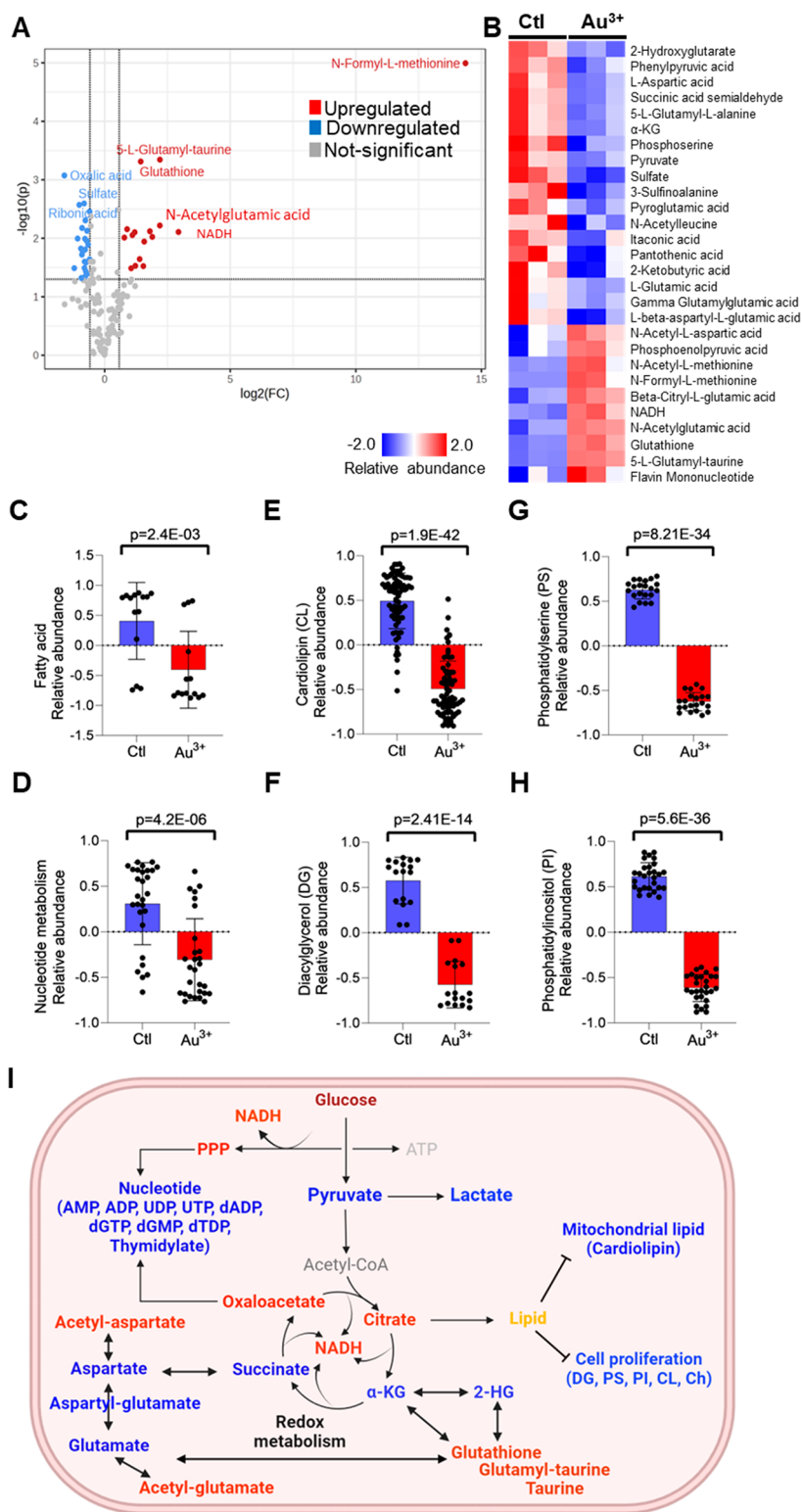


Figure 5. GNC biomineralization confers radiosensitization by modulating oxidative cancer metabolism and nucleotide synthesis. (A) Volcano plot showing significantly up- or downregulated metabolites in PANC1 cells after a 24 h treatment with 0.20 mM Au³⁺ compared to the untreated control (Au³⁺/Ctl). (B) Heatmap showing the relative abundance of metabolites in the TCA cycle and its antilepturic networks in PANC1 cells treated with 0.20 mM Au³⁺ relative to the untreated control. Levels of fatty acid (C), nucleotide (D), cardiolipin (CL) ($n = 75$) (E), diacylglycerol (DG) (F), phosphatidylserine (PS) (G), and phosphatidylinositol (PI) (H) in Au³⁺ treated and control PANC1 cells. (I) Metabolic perturbation through redox, oxidative, energy metabolism, and cell proliferation networks in PANC1 cells treated with 0.20 mM Au³⁺ compared to the control. Red color represents elevated abundance; blue color represents reduced abundance; gray color represents no changes; black color represents a biological process. All bar graph data are presented as mean values \pm standard deviation.

had intravascular tumor cell metastasis in the subcutaneous tissue near the tumor and focal subacute pyogranulomatous inflammation intermixed with atypical tumor-like cells into the mesentery. However, this and all other observed histopathologic lesions are subacute to chronic, which are older than 7 days, while Au³⁺ treatment was administered only 48 h prior to euthanasia and collection of tissue samples. Therefore, the observed local peritumoral and systemic immune inflammatory reactions were induced by the subcutaneous xenograft tumors with no significant difference between Au³⁺ treated and nontreated mice, which would support no toxicity of Au³⁺ treatment in these mice. Blood chemistry and hematology panels revealed no major differences between the Au³⁺-treated and sham treatment mice (Figure S8). The livers, gallbladders, lungs, kidneys, esophagi, hearts, skeletal muscles, aortas, and thymuses of the Au³⁺-treated mice and untreated mice did not differ significantly (Figure S9). However, Au³⁺-treated mice had a mildly higher serum globulin level and moderately higher white blood cell count (6.54×10^3) in comparison with untreated mice (3.98×10^3); these changes were not statistically significant ($P = 0.4554$). Of the white blood cells, both neutrophils ($P = 0.0452$) and lymphocytes ($P = 0.4116$) were higher in Au³⁺-treated mice (Figure S8). These results are consistent with the histopathological findings of lymphocytic hyperplasia in multiple lymphoid tissues (usually considered of little clinical significance)⁹⁰ and a compensatory increased extramedullary hematopoiesis in the spleen of these mice. Although this study could not accurately evaluate the toxicity of Au³⁺ treatment of tumors because of the local and systemic immune reaction induced by xenograft tumor cells, these data show no significant histopathologic differences between Au³⁺ treated and untreated mice, which suggest a minimal or no toxicity in mice with Au³⁺ treated tumors. Our plan is to carry out toxicity studies in normal mice next to eliminate confounding factors due to tumor presence and to complement the current studies.

Gold biodistribution was assessed by ICP-MS in PANC1 tumor xenografts 48 h after treatment with 1.0 mM Au³⁺, revealing that the amount of gold in the tumor at that time point was more than 10 times that in the liver, kidneys, spleen, lung, or heart (Figure 6A). Cryo-fluorescence tomography showed a fluorescence from GNCs in the Au³⁺-treated group that was absent in the untreated control group (Figure 6B). GNC fluorescence across multiple tumor cross sections did not fluctuate significantly, indicating a uniform distribution of GNCs in the tumor (Figure S10a,b).

We chose the 48 h time point based on previously published evaluations of temporal distribution and intratumoral clearance of Au³⁺ ions in subcutaneous murine xenograft tumor models^{58,65} that used GNC fluorescence as a tool to quantify these processes. These studies showed that the initiation of GNC formation occurs soon after Au³⁺ administration, peaking at ~24–48 h and, then, clearing at 7 days after the treatment. Further, our *in vitro* cell studies showed that GNC formation is saturated at ~24 h in PANC1 cells (Figure 2C). Therefore, we proceeded with the 48 h time point because it was identified as the longest time required to achieve the maximum GNC fluorescence.^{58,65} We would like to note that radiolabeling strategies for assessment of *in vivo* biodistribution that were reported for prefabricated GNP tracking^{91–93} cannot be employed for tracking Au³⁺ ions. However, previously reported use of a radioactive gold isotope ¹⁹⁸Au could provide an

opportunity to use nuclear imaging for *in vivo* monitoring of the *in situ* biomineralization.⁹⁴

TEM revealed particles of 3.5 ± 2.0 nm ($n = 156$ particles) in cellular nuclei (Figures 6C–E and S10c–e,h); these sizes were similar to those observed *in vitro* (i.e., 3.1 ± 1.8 nm) (Figure S2a). Further, larger GNPs of 10.3 ± 2.2 nm ($n = 259$) were detected along the collagen fibers (Figures 6F,G and S10f,g,i), which is consistent with reports of benchtop GNP synthesis mediated by the presence of collagen.^{95–97} Thus, our TEM studies revealed that gold biomineralization *in vivo* can also occur outside cancer cells (i.e., along collagen fibers); however, the intranuclear GNC formation *in vivo* was similar to that *in vitro*. Overall, the biodistribution analysis showed that *in situ* gold biomineralization enables a strong localization of GNCs and/or GNPs within the tumor relative to nontarget sites that is ideal for tumor-specific radiotherapy enhancement. Further, these *in situ* formed nanoparticles have sizes which are consistent with an efficient renal clearance.^{94,98}

Radiosensitization *in Vivo*. We used a tumor regrowth delay study and terminal survival analysis to determine radiosensitization *in vivo* in pancreatic tumor bearing mice receiving intratumoral injections of either PBS without radiation ($n = 10$), PBS with radiation ($n = 9$), Au³⁺ without radiation ($n = 10$), or Au³⁺ with radiation ($n = 10$). Tumor regrowth across a 38-day period following the treatments showed that the negative control, Au³⁺-only, and radiation-only groups had tumor doubling times of 21, 24, and 40 days, respectively. However, the tumors in the group treated with Au³⁺ and radiation did not exhibit a statistically significant change in volume ($P = 0.611$), indicating that the treatment effectively halted tumor growth (Figure 6H).

To compare tumor burden-induced mortality between treatment groups, we performed terminal survival analyses to identify and exclude events associated with nontarget competitive risks (i.e., not associated with tumor burden). These analyses indicated five mortality events that were not related to tumor burden and were thus excluded from the survival study (Supporting Materials and Figure S11). Survival analyses of mice whose mortality events were associated with tumor burden revealed that the median survival duration of the Au³⁺-plus-radiation group ($n = 7$; 235 days) was significantly longer than those of the nonirradiated control group ($n = 10$; 83 days), radiation-only group ($n = 7$; 102 days), and Au³⁺-only group ($n = 10$; 125.5 days) (Figure 6H). There were no statistically significant differences in survival between the control groups, indicating that Au³⁺ treatment or radiation alone were not able to provide significant relief.

CONCLUSIONS

Our findings demonstrate cancer radiosensitization through biosynthesis of GNCs and GNPs *in vitro* and *in vivo*. We found that intracellular gold biomineralization occurs with higher efficiency in cancerous versus noncancerous pancreatic cells and is associated with a strong nuclear localization of fluorescent GNCs, especially into nucleoli. We also showed that *in situ* biomineralized GNCs and GNPs radiosensitize pancreatic cancer cells by dysregulating DNA repair and cell metabolism and by accentuating peroxidation. We demonstrated that a radiosensitization strategy that relies on the delivery of an ultimately small precursor, Au³⁺ ion, for the *in situ* formation of GNCs and GNPs can significantly increase the efficiency of radiotherapy and provide survival benefits. This elegantly simple approach takes advantage of complex

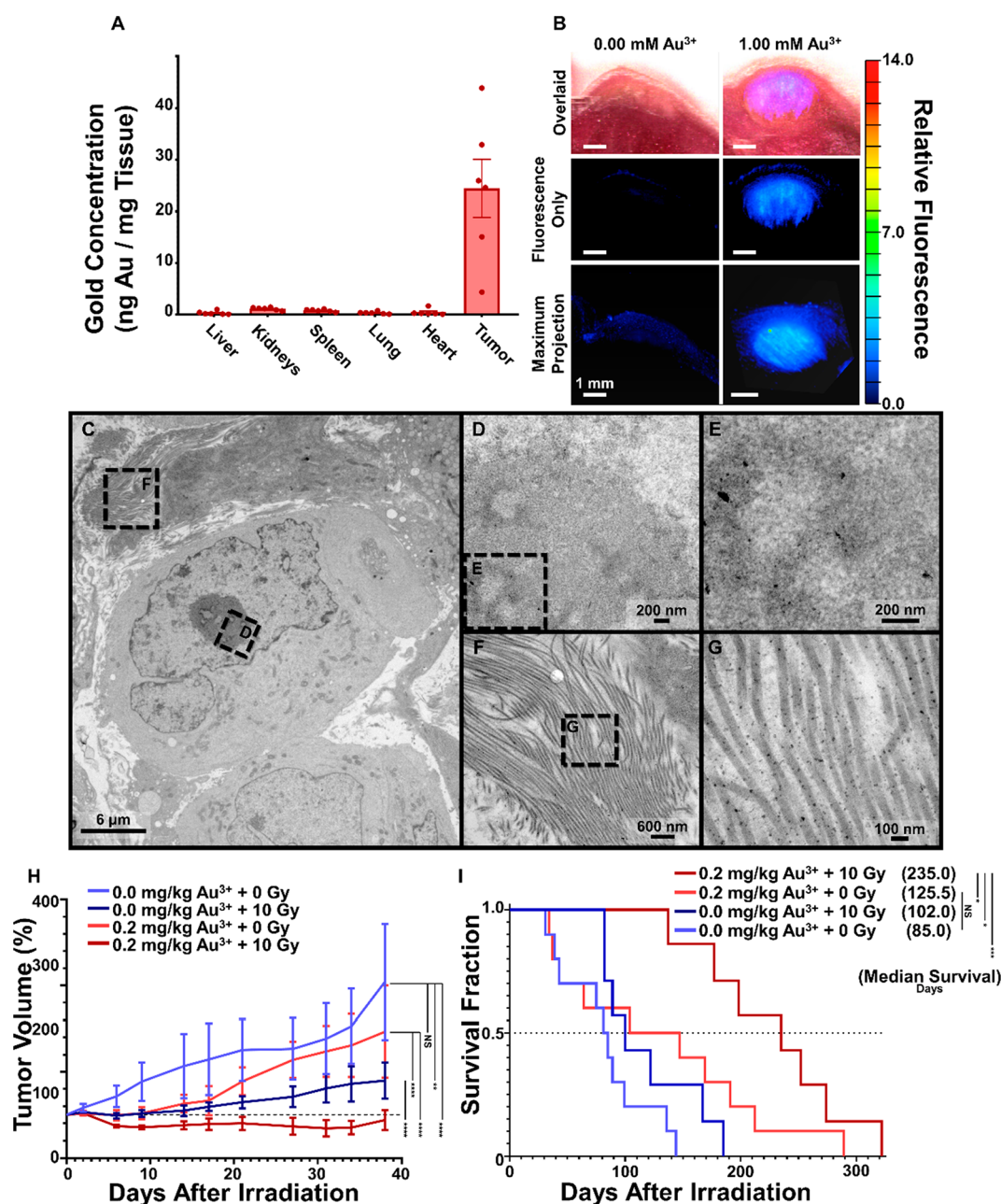


Figure 6. Intratumoral GNC biodistribution, biomineralization, and therapeutic radiosensitization effects. (A) ICP-MS analyses of gold content in the livers, kidneys, spleens, lungs, hearts, and tumors collected from nu/nu mice with left hind flank PANC1 tumor xenografts 48 h after intratumoral injections of 1.00 mM Au³⁺ in 20 μL of PBS. (B) Fluorescence ($\lambda_{\text{exc}}555 \text{ nm}/\lambda_{\text{em}}620 \text{ nm}$) and brightfield cryo-tomographic images (Emit Xerra) of PANC1 tumor xenografts 48 h after intratumoral injection of either 0.00 or 1.00 mM Au³⁺ in 20 μL of PBS. (C–G) TEM images of a PANC1 tumor xenograft harvested 48 h after intratumoral injection of 1.0 mM Au³⁺ in PBS (C), with magnified views of the nucleoli (D) and GNCs therein (E) as well as magnified views of collagen fibers (F) and GNPs therein (G). (H, I) Normalized tumor volume measurements (H) and survival fractions (I) over time for different treatments with Au³⁺ (0.0 or 0.2 mg/kg) and radiation (0 or 10 Gy). ^{NS}*P* > 0.05, **P* < 0.05, ***P* < 0.01, ****P* < 0.001, and *****P* < 0.0001.

biological machinery for intranuclear cancer targeting and does not require the sophisticated and potentially expensive synthesis of targeted nanoparticles. Interestingly, previously published reports demonstrated the possibility to control the size and morphology of *in situ* gold particle synthesis for application in photothermal therapy.^{63,65} In one study, a polyethylene glycol (PEG) coaggregation with gold ions was used to promote the formation of larger GNPs to increase the photothermal effect.⁶⁵ In another study, the authors were able to promote the formation of gold nanoribbons by adding

prefabricated GNPs to cells cotreated with gold ions.⁶³ The strategy utilizing a PEG nanovector for gold ion delivery could be more clinically relevant because it relies on delivery of a single entity whereas the other approach requires two components wherein the timing between their delivery is an essential component of the reaction's control. These studies indicate the feasibility of an engineering approach toward optimization of gold biomineralization for a specific biomedical application.

By obviating the need for systemic delivery, *in situ* gold biomineralization overcomes the challenge of evading reticuloendothelial capture of nanoparticles administered via the bloodstream and also avoids the need for nuclear transport moieties through the innate nuclear localization in cancer cells. Furthermore, our data show that this strategy can overcome delivery barriers associated with a dense tumor environment and cellular cytoplasmic and nuclear membranes. These studies could catalyze the future clinical translation of gold biomineralization for cancer radiotherapy.

METHODS

Cell Culture. PANC-1 and Mia-PaCa-2 cells were cultured according to ATCC guidelines in DMEM with 10% v/v FBS and 1× penicillin–streptomycin with the addition of 2.5% horse serum to the Mia-PaCa-2 cell media. HPDE cells were grown in keratinocyte serum-free complete media supplemented with 1× antibiotic–antimycotic. All cells were incubated under standard culture conditions (i.e., ~95% humidity, 5% CO₂, 37 °C, normal pH). Cells were passaged 2 or 3 times weekly using 0.25% trypsin–EDTA to prevent them from becoming overly confluent. In lifting HPDE cells, a trypsin inhibitor was used to quench trypsin activity before the cells were passaged to fresh culture dishes.

Intracellular GNC Biomineralization. A small volume (<1% of the total cell culture volume) of sterile filtered (using a 0.22 μm filter) chloroauric acid at a concentration of 50 or 100 mM (i.e., Au³⁺ mM) in Milli-Q water (18.2 MΩ) was added directly to the culture media. In a typical experiment, cells were grown in a T-75 cell culture flask up to 70–90% confluency ((6–8) × 10⁶ cells) before the treatment. Cells were incubated with Au³⁺ under normal cell culture conditions unless otherwise indicated. Treatments with supplementary cationic salts were administered in a sterile media in combination with the gold ion treatment. Sterile cell culture techniques were used throughout.

Confocal Microscopy. Cells were plated at 60–70% confluency in 8-well chambered coverglass slides (Lab-Tek) and allowed 24 h to adhere before treatment with Au³⁺. Cells were imaged using an SP8 Laser Scanning Confocal Microscope (Leica). A 561 nm excitation laser and a 610 ± 20 nm emission filter were used to detect GNC fluorescence using an avalanche photodiode photomultiplier tube detector. For the imaging of unstained cells, cells were treated with 1.00 mM Au³⁺ and allowed to incubate for 24 h before imaging. For the imaging of cells with nuclear staining, PANC1 cells were stained with Hoechst 33342 according to the manufacturer's protocol using Hoechst solution in PBS at 1:2000 dilution for 30 min followed by imaging within 30 min. The total nuclear GNC fluorescence per cell was quantified using Imaris software and the blue Hoechst 33342 channel to demarcate cell nuclei. For longitudinal imaging, we used an environmental imaging chamber attachment maintained at normal cell incubating conditions (i.e., ~95% humidity, 5% CO₂, 37 °C), and images were collected once every 10 min for 20 h.

TEM. Samples were fixed with a solution containing 3% glutaraldehyde plus 2% paraformaldehyde in 0.1 M cacodylate buffer, pH 7.3, then washed in 0.1 M sodium cacodylate buffer and treated with 0.1% Millipore-filtered cacodylate buffered tannic acid, postfixed with 1% buffered osmium tetroxide, and stained en bloc with 1% Millipore-filtered uranyl acetate. The samples were dehydrated in increasing concentrations of ethanol, infiltrated, and embedded in LX-112 medium. The samples were polymerized in a 60 °C oven for approximately 3 days. Ultrathin sections were cut in an Ultracut microtome (Leica), stained with uranyl acetate and lead citrate, and examined using a JEM 1010 transmission electron microscope (JEOL) at an accelerating voltage of 80 kV. Digital images were obtained using an imaging system from Advanced Microscopy Techniques.

Irradiation of Cells. For X-ray irradiation of cells, the plastic lids of irradiated plates were temporarily replaced with a clean parafilm seal in a sterile biosafety cabinet. The parafilm-sealed plates were

placed onto the bed of an XRAD SmART small animal irradiator (Precision XRay Inc.). A scout computed tomography (CT) scan was used to center the sample at the X-ray beam's isocenter within the field of view. A 4 cm × 4 cm square collimator was placed over the CT tube, and a 0.3 mm copper treatment filter was inserted. X-ray doses ranging from 2 to 10 Gy were delivered using an anterior–posterior treatment plan with a voltage of 225 kV and the current set to 20 mA.

MTS Assays. A CellTiter 96 AQueous Non-Radioactive Cell Proliferation Assay kit (Promega) was used according to the manufacturer's instructions. A detailed description is provided in the [Supporting Information](#).

JC-1 Assay. JC-1 mitochondrial membrane potential stain (Life Technologies) was prepared and used according to the manufacturer's instructions. A detailed description is provided in the [Supporting Information](#).

AO/PI Live–Dead Assay. Cells were seeded in T25 tissue culture flasks and incubated for approximately 24 h before Au³⁺ biomineralization treatments with chloroauric acid at final concentrations of 0.00, 0.10, or 0.20 mM Au. Cells were incubated with the Au³⁺ ions overnight followed by cell collection via trypsinization. Finally, cells were resuspended in PBS and briefly admixed with an Nexcelom AO/PI dye assay kit at a 1:1 (v/v) ratio immediately before 20 μL was dispensed to Cellometer Cell Counting Chambers for quantitation of viability using a Cellometer Auto 2000 Cell Viability Counter (Nexcelom) per the manufacturer's instructions.⁹⁹

Flow Cytometry. Cells were seeded in T75 tissue culture flasks at uniform density (60% confluency) and incubated for approximately 24 h before treatment with 0.20 mM Au³⁺ for 24 h; untreated cells were used as a control. After the treatment, the cells were washed with PBS, detached via trypsinization, washed with PBS, and stained with Hoechst 33342 according to the manufacturer's instructions. Then, the cells were washed with cold PBS (4 °C) by centrifugation (160g for 6 min); the cell pellet was resuspended in 500 μL of cold PBS, and the cells were immediately analyzed by flow cytometry using a 5-laser, 18-color LSRFortessa X-20 Analyzer (BD FACS Calibur, CA, USA). For each sample, 10,000 events were collected. The data were analyzed using FlowJo_v10.9.0 Software. Cell populations were gated using plots of side-scatter versus Hoechst intensity (355 nm excitation laser, 450/50 nm filter) to exclude debris, and histograms of the GNC channel intensities (561 nm excitation laser, 610/20 nm filter) were analyzed. The percentage of GNC positive cells was determined as the percentage of events in the treatment group that have a greater GNC intensity than the median plus robust σ of the untreated control, using methodology described in refs 100 and 101.

Clonogenic Survival Assay. PANC1 cells at approximately 70% confluency in T-75 culture flasks were treated with either 0.00 or 0.20 mM Au³⁺ and incubated for 24 h. The cells were then lifted with trypsinization, passaged to 35 mm tissue culture-treated dishes at concentrations ranging from 50 to 8,000 cells/plate ($n = 6$ replicates), and allowed to settle for 30–60 min before X-ray irradiation with 0, 2, 4, or 6 Gy. After irradiation, the cells were incubated in cell culture media for 14–21 days to form colonies. The colonies were washed with PBS and fixed with a 1:7 mixture of acetic acid and methanol. After fixation, the colonies were briefly stained with a 0.5% (g/g) crystal violet solution and washed with PBS, and the plates were placed upside-down to air-dry for 2 days. The colonies were imaged and manually counted using a UVP GelSolo gel documentation system (Analytik Jena). Plating efficiency and survival fractions were calculated using the procedure described by Franken et al.¹⁰²

γ-H2AX Foci Staining and Quantification. An Alexa Fluor 488-labeled γ-H2AX antibody (Fisher Scientific) was used to quantify double-stranded DNA breaks in cells treated with Au³⁺ and/or radiation. Cells were seeded in LabTek culture plate slides (#1.5) for 24 h to adhere before treatment with Au³⁺ and/or radiation. Following treatment, cells were washed with PBS three times, fixed with cold methanol (–20 °C) for no more than 30 min, and then washed three times with cold PBS (4 °C) containing 5% FBS. An Alexa Fluor-linked antibody in cold PBS with 5% FBS (1:2000 dilution) was added to the cells. Following overnight incubation at 4

°C, the cells were stained with Hoechst 33342 and imaged using an SP8 Laser Scanning Confocal Microscope (Leica) with a 488 nm excitation laser and a 610 ± 20 nm emission filter.

NADP/NADPH Quantification Assay. The NADP/NADPH quantification assay (MilliporeSigma) was performed according to the manufacturer's instructions. A detailed description is provided in the [Supporting Information](#).

TBARS Assay. The TBARS assay (MilliporeSigma) was performed according to the manufacturer's instructions. A detailed description is provided in the [Supporting Information](#).

Nontargeted Metabolomics. To determine the relative abundance of polar metabolites in cell samples, extracts were prepared and analyzed by ultrahigh resolution mass spectrometry (HRMS). Metabolites were extracted using ice-cold 0.1% ammonium hydroxide in 80/20 (v/v) methanol/water. Extracts were centrifuged at 17,000g for 5 min at 4 °C, and supernatants were transferred to clean tubes, followed by evaporation to dryness under nitrogen. Dried extracts were reconstituted in deionized water, and 5 μ L was injected for analysis by ion chromatography (IC)-MS. IC mobile phase A (MPA; weak) was water, and mobile phase B (MPB; strong) was water containing 100 mM KOH. A Thermo Scientific Dionex ICS-5000+ system included a Thermo IonPac AS11 column (4 μ m particle size, 250 \times 2 mm) with the column compartment kept at 30 °C. The autosampler tray was chilled to 4 °C. The mobile phase flow rate was 350 μ L/min, and a gradient from 1 to 100 mM KOH was used. The total run time was 60 min. To assist the desolvation for better sensitivity, methanol was delivered by an external pump and combined with the eluent via a low dead volume mixing tee. Data were acquired using a Thermo Orbitrap Fusion Tribrid Mass Spectrometer under ESI negative ionization mode at a resolution of 240,000.

Nontargeted Lipidomics. To determine the relative abundance of lipid in PANC1 cells, extracts were prepared and analyzed by the high-resolution mass spectrometry-based lipidomics at the MD Anderson Cancer Center Metabolomics Core Facility. Briefly, to each cell sample, 200 μ L of extraction solution containing 2% Avanti SPLASH LIPIDOMIX Mass Spec Standard and 1% 10 mM butylated hydroxytoluene in ethanol was added, and the tubes were vortexed 10 min. The tubes sat in ice for 10 min and were centrifuged at 13,300 rpm for 10 min at 4 °C. The supernatant was transferred to a glass autosampler vial, and the injection volume was 10 μ L. Mobile phase A (MPA) was 40:60 acetonitrile:water with 0.1% formic acid and 10 mM ammonium formate. Mobile phase B (MPB) was 90:9:1 isopropanol:acetonitrile:water with 0.1% formic acid and 10 mM ammonium formate. The chromatographic method included a Thermo Fisher Scientific Accucore C30 column (2.6 μ m, 150 \times 2.1 mm) maintained at 40 °C, autosampler tray chilled at 8 °C, a mobile phase flow rate of 0.200 mL/min, and a gradient elution program as follows: 0–3 min, 30% MPB; 3–13 min, 30–43% MPB; 13.1–33 min, 50–70% MPB; 48–55 min, 99% MPB; 55.1–60 min, 30% MPB.

A Thermo Fisher Scientific Orbitrap Fusion Lumos Tribrid mass spectrometer with heated electrospray ionization source was operated in data dependent acquisition mode, in both positive and negative ionization modes, with scan ranges of 150–827 and 825–1500 *m/z*. An Orbitrap resolution of 120,000 (fwhm) was used for MS1 acquisition and spray voltages of 3,600 and –2,900 V were used for positive and negative ionization modes, respectively. Vaporizer and ion transfer tube temperatures were set at 275 and 300 °C, respectively. The sheath, auxiliary, and sweep gas pressures were 35, 10, and 0 (arbitrary units), respectively. For MS² and MS³ fragmentation, a hybridized HCD/CID approach was used. Each sample was analyzed using four injections making use of the two aforementioned scan ranges, in both ionization modes. Data were analyzed using Thermo Scientific LipidSearch software (version 5.0) and R scripts written in house.

Xenograft Implantation and Gold Treatment Administration. PANC-1 cells determined to be negative for mycoplasma by MD Anderson's Cytogenetics and Cell Authentication Core were used. All animal protocols were approved by MD Anderson's Institutional Animal Care and Use Committee. For xenograft

implantation, approximately 2×10^6 cells/100 μ L sterile filtered PBS were admixed with an equivalent volume of Matrigel, resulting in approximately 1×10^6 cells/100 μ L injection suspension. Fifty microliters of the cell suspension ($\sim 0.5 \times 10^6$ cells) was injected subcutaneously into the left hind flanks of nu/nu mice under isoflurane anesthesia using a 30G needle. Intratumoral injections of Au³⁺ were performed when tumors reached approximately 70 mm³ (~ 50 days after cell implantation). The mice were given 20 μ L intratumoral injections of either sterile filtered phosphate-buffered saline (PBS) or 1.00 mM Au³⁺ in PBS (i.e., ~ 0.2 mg Au/kg mouse weight). We chose direct intratumoral injection as the delivery approach because of the hypovascular nature of pancreatic cancer and as a means of penetrating stroma without disrupting it. Furthermore, recent clinical studies showed that intratumorally administered TNFerade¹⁰³ and functionalized hafnium oxide nanoparticles⁴ are well-tolerated and feasible options in the treatment of pancreatic ductal adenocarcinoma.

Histopathological Evaluation. Xenograft tumor-bearing mice were euthanized 48 h after intratumoral Au³⁺ treatment, and tissue samples from the liver, kidney, lung, trachea, heart, aorta, spleen, mesenteric lymph node, thymus, esophagus, and tumor xenograft were fixed in 10% neutral buffered formalin solution for 72 h. Formalin-fixed tissues were embedded in paraffin blocks, sectioned, and stained with hematoxylin and eosin (H&E) for histopathological evaluation by a board-certified veterinary pathologist. Microscopic examination of histologic sections was performed using an Olympus BX41 microscope coupled to a Leica DFC495 camera. Histologic changes or lesions were recorded and scored for extent and severity.

Blood Chemistry and Hematology Analysis. Blood samples were collected immediately after euthanasia via cardiocentesis into microtubes containing either EDTA for the hematology analysis or a serum separator for the blood chemistry analysis. Within 4 h of sample collection, complete blood counts were analyzed with the ADVIA 120 Hematology System (Siemens). Blood chemistry, including serum levels of albumin, alkaline phosphatase, alanine transaminase, aspartate transaminase, blood urea nitrogen, creatinine, globulin, and total protein, was analyzed using the COBAS INTEGRA 400 Plus system (Roche).

Quantification of Gold. The elemental gold content in the *in vitro* and *in vivo* samples treated with chloroauric acid was quantified using a NexION 2000B ICP-MS system (PerkinElmer) after sample preparation with the hot plate dissolution technique using TraceMetal grade concentrated acids. The tissue samples were vacuum-dried for >48 h, accurately weighed, and then solubilized by treatment with 67–69% nitric acid (Fisher A467-1) and 35–38% hydrochloric acid (Fisher A466-1) under a fume hood. First, 2.5 mL of nitric acid was added to samples for 24 h at room temperature. Then, 0.5 mL of hydrochloric acid was added, and the vial was closed using a screw cap with a preslit polytetrafluoroethylene liner and kept on top of a hot plate at 90 °C for 96–480 h, until the liquid inside became completely clear. The vial was cooled to room temperature, and the cap was carefully removed. The open vial was placed on top of a hot plate at 120 °C until the volume reduced to approximately 0.5 mL. The residue was diluted with a solution of 1% nitric acid and 3% hydrochloric acid in deionized water to the final volume of 10 mL. The resulting solution was then filtered through 0.2 μ m glass microfiber syringe filters into a 15 mL PP Eppendorf tube. For ICP-MS, a glass cyclonic sample introduction system was used along with a SMARTintro sample introduction cassette (Blue) with a 2.0 mm fixed injector and a MEINHARD concentric nebulizer. Settings used for ICP-MS samples were as follows: nebulizer flow rate, 1.14 L/min; plasma gas flow rate, 18 L/min; radiofrequency power, 1600 W; dwell time, 30 μ s; helium reaction gas flow rate, 1.5 mL/min. Each sample was followed by a blank to eliminate any measurement inconsistencies due to gold carryover (i.e., instrument memory effect). Before the analysis, the instrument was optimized using the automated SmartTune procedure targeting maximum gold sensitivity (Syngistix ICP-MS software, v.2.5.1904.21469). Gold concentrations were calculated from a regression equation built with a set of standards with concentrations of 1×10^{-10} to 1×10^{-4} g/L prepared by diluting

the gold primary standard (TraceCERT, 1000 mg/L). A 0.10 $\mu\text{g/L}$ Ga^{3+} internal standard was added to the blank, all calibration standards, and all samples. The Ga^{3+} standard was prepared by diluting the gallium primary standard (1000 mg/L, Specpure) in a polypropylene volumetric flask to the desired volume with 2% hydrochloric acid in deionized water.

Xerra Cryo-Tomographic Fluorescence Imaging. All mice were handled in accordance with MD Anderson's Institutional Animal Care and Use Committee guidelines. Immediately after euthanasia, mice were frozen by dipping them head-first into hexane cooled with dry ice and then stored at $-20\text{ }^\circ\text{C}$ for no more than 2 weeks before they were embedded in optimum cutting temperature compound using a special mold designed for Xerra imaging. The embedded mice were affixed to the Xerra stage using a screw mechanism. The Xerra imaging protocol included both white light and fluorescence imaging ($\lambda_{\text{ex}}555\text{ nm}/\lambda_{\text{em}}620\text{ nm}$) with a $50\text{ }\mu\text{m}$ slice thickness. The imaging data were reconstructed, normalized, and extracted using the Emit software program. Pixel fluorescence intensity values for tumor slices were analyzed using ImageJ, with the intensity values normalized by the corresponding exposure times.

Irradiation of Tumor Xenografts. Radiotherapy was administered 48 h after intratumoral injections of either 20 μL sterile filtered PBS (negative control; $n = 17$) or 1.00 mM Au^{3+} in PBS ($n = 20$). A single dose of 10 Gy was administered to mice treated with either PBS (radiation only; $n = 7$) or Au^{3+} (radiation plus Au^{3+} ; $n = 10$); 10 mice were used as an untreated control (i.e., PBS injection only) group, and 10 mice were used as a Au^{3+} treatment group (i.e., Au^{3+} injection only). Mice were anesthetized using 2% isoflurane and placed onto the bed of an XRAD SmART small animal irradiator (Precision XRay Inc.). A scout CT scan was used to center the tumor at the beam isocenter within the field of view. A 1.5 cm collimator was placed over the CT tube, and a 0.3 mm copper treatment filter was inserted. A 10 Gy dose was delivered using an anterior–posterior/posterior–anterior treatment plan. The anterior–posterior beam time was 71 s, and the posterior–anterior beam time was 78 s. The voltage used was 225 kV, and the current was set to 20 mA. All mice recovered in a warm clean cage after irradiation.

Weight and Tumor Volume Measurements. Following tumor implantation, mouse weight and tumor volume were assessed weekly using a gram scale and caliper measurements, respectively. After X-ray irradiation, tumor size and mouse weight were collected twice a week. Tumor volume was calculated using the equation $V = L \times W \times W$, where L is the larger dimension and W is the smaller. Mice were euthanized with CO_2 asphyxiation followed by cervical dislocation if they had $\geq 20\%$ weight loss from baseline, a tumor burden exceeding 2 cm in any dimension, or any other major health issues.

ASSOCIATED CONTENT

Supporting Information

The Supporting Information is available free of charge at <https://pubs.acs.org/doi/10.1021/acsnano.3c04260>.

Optimization of treatment conditions for intracellular gold nanocluster biomineralization (S1.1.), competitive risk events in survival studies (S1.2.), materials used (S1.3.), and detailed kit assay methods (S1.4.); confocal fluorescence images; analysis of cellular TEM and optical properties of albumin-coated GNCs; gold nanoparticle biosynthesis and cell viability; cell viability and ROS induction by physiological cationic ions; uptake of gold ions; formation of peroxidation products; biochemistry and hematology analysis; histology of normal organs; intratumoral GNC biomineralization; analysis of competitive risk events; assay calibration plots; histopathology evaluation results (PDF)

Movie S1: gold nanocluster (GNC) formation inside live PANC1 cells over a period of 20 h; acquired every 10 min using confocal fluorescence microscopy with a 561

nm excitation laser and a $610 \pm 20\text{ nm}$ emission filter to detect GNC fluorescence (red); under standard culture conditions (i.e., $\sim 95\%$ humidity, 5% CO_2 , $37\text{ }^\circ\text{C}$, normal pH) (MP4)

AUTHOR INFORMATION

Corresponding Authors

Sunil Krishnan – Vivian L. Smith Department of Neurosurgery, University of Texas Health Science Center, Houston, Texas 77030, United States; Email: krishnan.sunil@uth.tmc.edu

Konstantin V. Sokolov – Department of Imaging Physics, The University of Texas MD Anderson Cancer Center, Houston, Texas 77030, United States; orcid.org/0000-0002-0198-2005; Email: ksokolov@mdanderson.org

Authors

Aaron S. Schwartz-Duval – Department of Imaging Physics, The University of Texas MD Anderson Cancer Center, Houston, Texas 77030, United States; orcid.org/0000-0001-6819-7418

Yuri Mackeyev – Vivian L. Smith Department of Neurosurgery, University of Texas Health Science Center, Houston, Texas 77030, United States

Iqbal Mahmud – Department of Bioinformatics and Computational Biology, The University of Texas MD Anderson Cancer Center, Houston, Texas 77030, United States; orcid.org/0000-0001-7729-8122

Philip L. Lorenzi – Department of Bioinformatics and Computational Biology, The University of Texas MD Anderson Cancer Center, Houston, Texas 77030, United States; orcid.org/0000-0003-0385-7774

Mihai Gagea – Department of Veterinary Medicine & Surgery, The University of Texas MD Anderson Cancer Center, Houston, Texas 77030, United States

Complete contact information is available at: <https://pubs.acs.org/doi/10.1021/acsnano.3c04260>

Author Contributions

The manuscript was written through contributions of all authors. Conceptualization of the work was by A.S.S.-D., S.K., and K.V.S.; methodology design by A.S.S.-D., Y.M., I.M., P.L.L., M.G., S.K., and K.V.S.; investigation carried out by A.S.S.-D., Y.M., I.M., P.L.L., and M.G.; visualization of data by A.S.S.-D., I.M., P.L.L., and M.G.; supervision by S.K. and K.V.S.; writing of the original draft carried out by A.S.S.-D., Y.M., I.M., P.L.L., M.G., S.K., and K.V.S.; the review and editing done by A.S.S.-D., Y.M., I.M., P.L.L., M.G., S.K., and K.V.S. All authors have given approval to the final version of the manuscript.

Funding

This work was supported by the National Institutes of Health (NIH) through grants to K.V.S. (R21CA252156 and R01CA274415) and S.K. (R21CA252156, R01CA257241, and R01DE028105). A.S.S.-D. was supported by a fellowship funded by an NIH Institutional National Research Service Award (T32 CA196561).

Notes

The authors declare no competing financial interest. A preprint version of these studies was submitted to the ChemRxiv server.¹⁰⁴

ACKNOWLEDGMENTS

This work used MD Anderson's High-Resolution Electron Microscopy Facility (supported in part by NIH P30CA016672), Advanced Microscopy Core (NIH S10RR029552), Department of Veterinary Medicine and Surgery Veterinary Pathology Services, Cytogenetics and Cell Authentication Core (NIH P30CA016672), Small Animal Imaging Facility (NIH P30CA016672), Flow Cytometry and Cellular Imaging Core Facility (P30CA16672), and Metabolomics Facility (supported in part by Cancer Prevention Research Institute of Texas [CPRIT] grant number RP130397 and NIH grants S10OD012304-01, U01CA235510, and P30CA016672). We thank Joe Munch in MD Anderson's Research Medical Library for editing the manuscript and Dmitry Nevozhay, Department of Imaging Physics, M.D. Anderson Cancer Center, for fruitful discussions of statistical analysis of survival studies.

ABBREVIATIONS

GNP, gold nanoparticle; GNC, gold nanocluster; Au³⁺, ionic gold from chloroauric acid; TEM, transmission electron microscopy; FBS, fetal bovine serum; ICP-MS, inductively coupled plasma mass spectrometry; JC-1, tetraethylbenzimidazolylcarbocyanine iodide; NADP, nicotinamide adenine dinucleotide phosphate; TBARS, thiobarbituric acid reactive substance; CT, computed tomography; PBS, phosphate-buffered saline; H&E, hematoxylin and eosin; UHPLC-HRMS, ultrahigh resolution mass spectrometry

REFERENCES

- (1) Huguet, F.; Goodman, K. A.; Azria, D.; Racadot, S.; Abrams, R. A. Radiotherapy technical considerations in the management of locally advanced pancreatic cancer: American-French consensus recommendations. *International journal of radiation oncology, biology, physics* **2012**, *83* (5), 1355–64.
- (2) Krishnan, S.; Chadha, A. S.; Suh, Y.; Chen, H. C.; Rao, A.; Das, P.; Minsky, B. D.; Mahmood, U.; Deldos, M. E.; Sawakuchi, G. O.; Beddar, S.; Katz, M. H.; Fleming, J. B.; Javle, M. M.; Varadhachary, G. R.; Wolff, R. A.; Crane, C. H. Focal Radiation Therapy Dose Escalation Improves Overall Survival in Locally Advanced Pancreatic Cancer Patients Receiving Induction Chemotherapy and Consolidative Chemoradiation. *International journal of radiation oncology, biology, physics* **2016**, *94* (4), 755–65.
- (3) Reyngold, M.; O'Reilly, E. M.; Varghese, A. M.; Fiasconaro, M.; Zinovoy, M.; Romesser, P. B.; Wu, A.; Hajj, C.; Cuaron, J. J.; Tuli, R.; Hilal, L.; Khalil, D.; Park, W.; Yorke, E. D.; Zhang, Z.; Yu, K. H.; Crane, C. H. Association of Ablative Radiation Therapy With Survival Among Patients With Inoperable Pancreatic Cancer. *JAMA Oncol* **2021**, *7* (5), 735–738.
- (4) Bagley, A. F.; Ludmir, E. B.; Maitra, A.; Minsky, B. D.; Smith, G. L.; Das, P.; Koong, A. C.; Holliday, E. B.; Taniguchi, C. M.; Katz, M. H. NBTXR3, a first-in-class radioenhancer for pancreatic ductal adenocarcinoma: report of first patient experience. *Clinical and Translational Radiation Oncology* **2022**, *33*, 66–69.
- (5) Lee, J.; Chatterjee, D. K.; Lee, M. H.; Krishnan, S. Gold nanoparticles in breast cancer treatment: Promise and potential pitfalls. *Cancer Lett.* **2014**, *347* (1), 46–53.
- (6) Leung, M. K. K.; Chow, J. C. L.; Chithrani, B. D.; Lee, M. J. G.; Oms, B.; Jaffray, D. A. Irradiation of gold nanoparticles by x-rays: Monte Carlo simulation of dose enhancements and the spatial properties of the secondary electrons production. *Med. Phys.* **2011**, *38* (2), 624–631.
- (7) Lechtman, E.; Mashouf, S.; Chattopadhyay, N.; Keller, B. M.; Lai, P.; Cai, Z.; Reilly, R. M.; Pignol, J. P. A Monte Carlo-based model of gold nanoparticle radiosensitization accounting for increased radiobiological effectiveness. *Phys. Med. Biol.* **2013**, *58* (10), 3075–3087.
- (8) Ngwa, W.; Makrigrigios, G. M.; Berbeco, R. I. Applying gold nanoparticles as tumor-vascular disrupting agents during brachytherapy: estimation of endothelial dose enhancement. *Phys. Med. Biol.* **2010**, *55* (21), 6533–6548.
- (9) Zygmanski, P.; Liu, B.; Tsiamas, P.; Cifter, F.; Petersheim, M.; Hesser, J.; Sajo, E. Dependence of Monte Carlo microdosimetric computations on the simulation geometry of gold nanoparticles. *Phys. Med. Biol.* **2013**, *58* (22), 7961–7977.
- (10) Cho, S. H.; Jones, B. L.; Krishnan, S. The dosimetric feasibility of gold nanoparticle-aided radiation therapy (GNRT) via brachytherapy using low-energy gamma-/x-ray sources. *Phys. Med. Biol.* **2009**, *54* (16), 4889–4905.
- (11) Jones, B. L.; Krishnan, S.; Cho, S. H. Estimation of microscopic dose enhancement factor around gold nanoparticles by Monte Carlo calculations. *Med. Phys.* **2010**, *37* (7), 3809–3816.
- (12) Schuermann, J.; Bagley, A. F.; Berbeco, R.; Bromma, K.; Butterworth, K. T.; Byrne, H. L.; Chithrani, B. D.; Cho, S. H.; Cook, J. R.; Favaudon, V. Roadmap for metal nanoparticles in radiation therapy: Current status, translational challenges, and future directions. *Physics in Medicine & Biology* **2020**, *65* (21), 21RM02.
- (13) McMahon, S. J.; Hyland, W. B.; Muir, M. F.; Coulter, J. A.; Jain, S.; Butterworth, K. T.; Schettino, G.; Dickson, G. R.; Hounsell, A. R.; O'sullivan, J. M. Biological consequences of nanoscale energy deposition near irradiated heavy atom nanoparticles. *Sci. Rep.* **2011**, *1* (1), 1–10.
- (14) Izci, M.; Maksudian, C.; Manshian, B. B.; Soenen, S. J. The use of alternative strategies for enhanced nanoparticle delivery to solid tumors. *Chem. Rev.* **2021**, *121* (3), 1746–1803.
- (15) Wilhelm, S.; Tavares, A. J.; Dai, Q.; Ohta, S.; Audet, J.; Dvorak, H. F.; Chan, W. C. Analysis of nanoparticle delivery to tumours. *Nature reviews materials* **2016**, *1* (5), 1–12.
- (16) Ouyang, B.; Poon, W.; Zhang, Y.-N.; Lin, Z. P.; Kingston, B. R.; Tavares, A. J.; Zhang, Y.; Chen, J.; Valic, M. S.; Syed, A. M. The dose threshold for nanoparticle tumour delivery. *Nature materials* **2020**, *19* (12), 1362–1371.
- (17) Golombek, S. K.; May, J.-N.; Theek, B.; Appold, L.; Drude, N.; Kiessling, F.; Lammers, T. Tumor targeting via EPR: Strategies to enhance patient responses. *Advanced drug delivery reviews* **2018**, *130*, 17–38.
- (18) Sykes, E. A.; Dai, Q.; Sarsons, C. D.; Chen, J.; Rocheleau, J. V.; Hwang, D. M.; Zheng, G.; Cramb, D. T.; Rinker, K. D.; Chan, W. C. Tailoring nanoparticle designs to target cancer based on tumor pathophysiology. *Proc. Natl. Acad. Sci. U. S. A.* **2016**, *113* (9), E1142–E1151.
- (19) Tsoi, K. M.; MacParland, S. A.; Ma, X.-Z.; Spetzler, V. N.; Echeverri, J.; Ouyang, B.; Fadel, S. M.; Sykes, E. A.; Goldaracena, N.; Kathis, J. M. Mechanism of hard-nanomaterial clearance by the liver. *Nature materials* **2016**, *15* (11), 1212–1221.
- (20) Sindhwanji, S.; Syed, A. M.; Ngai, J.; Kingston, B. R.; Maiorino, L.; Rothschild, J.; MacMillan, P.; Zhang, Y.; Rajesh, N. U.; Hoang, T. The entry of nanoparticles into solid tumours. *Nature materials* **2020**, *19* (5), 566–575.
- (21) Maeda, H.; Khatami, M. Analyses of repeated failures in cancer therapy for solid tumors: poor tumor-selective drug delivery, low therapeutic efficacy and unsustainable costs. *Clinical and translational medicine* **2018**, *7* (1), 20.
- (22) Ojha, T.; Pathak, V.; Shi, Y.; Hennink, W. E.; Moonen, C. T.; Storm, G.; Kiessling, F.; Lammers, T. Pharmacological and physical vessel modulation strategies to improve EPR-mediated drug targeting to tumors. *Advanced drug delivery reviews* **2017**, *119*, 44–60.
- (23) Li, S.-D.; Huang, L. Pharmacokinetics and biodistribution of nanoparticles. *Mol. Pharmaceutics* **2008**, *5* (4), 496–504.
- (24) Goddard, Z. R.; Marin, M. J.; Russell, D. A.; Searcey, M. Active targeting of gold nanoparticles as cancer therapeutics. *Chem. Soc. Rev.* **2020**, *49* (23), 8774–8789.

- (25) Byrne, J. D.; Betancourt, T.; Brannon-Peppas, L. Active targeting schemes for nanoparticle systems in cancer therapeutics. *Advanced drug delivery reviews* **2008**, *60* (15), 1615–1626.
- (26) Dai, Q.; Wilhelm, S.; Ding, D.; Syed, A. M.; Sindhiani, S.; Zhang, Y.; Chen, Y. Y.; MacMillan, P.; Chan, W. C. Quantifying the ligand-coated nanoparticle delivery to cancer cells in solid tumors. *ACS Nano* **2018**, *12* (8), 8423–8435.
- (27) Liu, M.; Song, W.; Huang, L. Drug delivery systems targeting tumor-associated fibroblasts for cancer immunotherapy. *Cancer letters* **2019**, *448*, 31–39.
- (28) Liu, Y.; Guo, J.; Huang, L. Modulation of tumor microenvironment for immunotherapy: focus on nanomaterial-based strategies. *Theranostics* **2020**, *10* (7), 3099.
- (29) Peiris, P. M.; He, F.; Covarrubias, G.; Raghunathan, S.; Turan, O.; Lorkowski, M.; Gnanasambandam, B.; Wu, C.; Schiemann, W.; Karathanasis, E. Precise targeting of cancer metastasis using multi-ligand nanoparticles incorporating four different ligands. *Nanoscale* **2018**, *10* (15), 6861–6871.
- (30) Colombo, M.; Fiandra, L.; Alessio, G.; Mazzucchelli, S.; Nebuloni, M.; De Palma, C.; Kantner, K.; Pelaz, B.; Rotem, R.; Corsi, F. Tumour homing and therapeutic effect of colloidal nanoparticles depend on the number of attached antibodies. *Nat. Commun.* **2016**, *7* (1), No. 13818.
- (31) Rao, L.; Meng, Q.-F.; Bu, L.-L.; Cai, B.; Huang, Q.; Sun, Z.-J.; Zhang, W.-F.; Li, A.; Guo, S.-S.; Liu, W. Erythrocyte membrane-coated upconversion nanoparticles with minimal protein adsorption for enhanced tumor imaging. *ACS Appl. Mater. Interfaces* **2017**, *9* (3), 2159–2168.
- (32) Gao, W.; Hu, C.-M. J.; Fang, R. H.; Luk, B. T.; Su, J.; Zhang, L. Surface functionalization of gold nanoparticles with red blood cell membranes. *Advanced materials (Deerfield Beach, Fla.)* **2013**, *25* (26), 3549.
- (33) Xuan, M.; Shao, J.; Dai, L.; Li, J.; He, Q. Macrophage cell membrane camouflaged Au nanoshells for in vivo prolonged circulation life and enhanced cancer photothermal therapy. *ACS Appl. Mater. Interfaces* **2016**, *8* (15), 9610–9618.
- (34) Parodi, A.; Quattrocchi, N.; Van De Ven, A. L.; Chiappini, C.; Evangelopoulos, M.; Martinez, J. O.; Brown, B. S.; Khaled, S. Z.; Yazdi, I. K.; Enzo, M. V. Synthetic nanoparticles functionalized with biomimetic leukocyte membranes possess cell-like functions. *Nature Nanotechnol.* **2013**, *8* (1), 61–68.
- (35) Krishnamurthy, S.; Gnanasamandhan, M.; Xie, C.; Huang, K.; Cui, M.; Chan, J. Monocyte cell membrane-derived nanohosts for targeted cancer therapy. *Nanoscale* **2016**, *8* (13), 6981–6985.
- (36) Glinsky, V. V.; Glinsky, G. V.; Glinskii, O. V.; Huxley, V. H.; Turk, J. R.; Mossine, V. V.; Deutscher, S. L.; Pienta, K. J.; Quinn, T. P. Intravascular metastatic cancer cell homotypic aggregation at the sites of primary attachment to the endothelium. *Cancer research* **2003**, *63* (13), 3805–3811.
- (37) Zhu, J.-Y.; Zheng, D.-W.; Zhang, M.-K.; Yu, W.-Y.; Qiu, W.-X.; Hu, J.-J.; Feng, J.; Zhang, X.-Z. Preferential cancer cell self-recognition and tumor self-targeting by coating nanoparticles with homotypic cancer cell membranes. *Nano Lett.* **2016**, *16* (9), 5895–5901.
- (38) Rao, L.; Yu, G. T.; Meng, Q. F.; Bu, L. L.; Tian, R.; Lin, L. S.; Deng, H.; Yang, W.; Zan, M.; Ding, J. Cancer cell membrane-coated nanoparticles for personalized therapy in patient-derived xenograft models. *Adv. Funct. Mater.* **2019**, *29* (51), 1905671.
- (39) Stewart, A.; Urbaniak, S.; Turner, M.; Bessos, H. The application of a new quantitative assay for the monitoring of integrin-associated protein CD47 on red blood cells during storage and comparison with the expression of CD47 and phosphatidylserine with flow cytometry. *Transfusion* **2005**, *45* (9), 1496–1503.
- (40) Kriebardis, A. G.; Antonelou, M. H.; Stamoulis, K. E.; Economou-Petersen, E.; Margaritis, L. H.; Papassideri, I. S. RBC-derived vesicles during storage: ultrastructure, protein composition, oxidation, and signaling components. *Transfusion* **2008**, *48* (9), 1943–1953.
- (41) Liu, H.; Su, Y.-Y.; Jiang, X.-C.; Gao, J.-Q. Cell membrane-coated nanoparticles: a novel multifunctional biomimetic drug delivery system. *Drug Delivery and Translational Research* **2023**, *13* (3), 716–737.
- (42) Fang, R. H.; Kroll, A. V.; Gao, W.; Zhang, L. Cell membrane coating nanotechnology. *Adv. Mater.* **2018**, *30* (23), No. 1706759.
- (43) Hu, C.-M. J.; Zhang, L.; Aryal, S.; Cheung, C.; Fang, R. H.; Zhang, L. Erythrocyte membrane-camouflaged polymeric nanoparticles as a biomimetic delivery platform. *Proc. Natl. Acad. Sci. U. S. A.* **2011**, *108* (27), 10980–10985.
- (44) Hu, C.-M. J.; Fang, R. H.; Wang, K.-C.; Luk, B. T.; Thamphiwatana, S.; Dehaini, D.; Nguyen, P.; Angsantikul, P.; Wen, C. H.; Kroll, A. V. Nanoparticle biointerfacing by platelet membrane cloaking. *Nature* **2015**, *526* (7571), 118–121.
- (45) Xu, R.; Rai, A.; Chen, M.; Suwakulsiri, W.; Greening, D. W.; Simpson, R. J. Extracellular vesicles in cancer—implications for future improvements in cancer care. *Nature reviews Clinical oncology* **2018**, *15* (10), 617–638.
- (46) Lener, T.; Gimona, M.; Aigner, L.; Börger, V.; Buzas, E.; Camussi, G.; Chaput, N.; Chatterjee, D.; Court, F. A.; Portillo, H. A. d. Applying extracellular vesicles based therapeutics in clinical trials—an ISEV position paper. *Journal of extracellular vesicles* **2015**, *4* (1), No. 30087.
- (47) Piffoux, M.; Silva, A. K.; Lugagne, J. B.; Hersen, P.; Wilhelm, C.; Gazeau, F. Extracellular vesicle production loaded with nanoparticles and drugs in a trade-off between loading, yield and purity: towards a personalized drug delivery system. *Advanced Biosystems* **2017**, *1* (5), No. 1700044.
- (48) Tofilon, P. J.; Camphausen, K. Molecular targets for tumor radiosensitization. *Chem. Rev.* **2009**, *109* (7), 2974–2988.
- (49) Özçelik, S.; Pratz, G. Nuclear-targeted gold nanoparticles enhance cancer cell radiosensitization. *Nanotechnology* **2020**, *31* (41), No. 415102.
- (50) Jain, R. K.; Stylianopoulos, T. Delivering nanomedicine to solid tumors. *Nat. Rev. Clin. Oncol.* **2010**, *7* (11), 653–64.
- (51) Ozdemir, B. C.; Pentcheva-Hoang, T.; Carstens, J. L.; Zheng, X.; Wu, C. C.; Simpson, T. R.; Laklai, H.; Sugimoto, H.; Kahlert, C.; Novitskiy, S. V.; De Jesus-Acosta, A.; Sharma, P.; Heidari, P.; Mahmood, U.; Chin, L.; Moses, H. L.; Weaver, V. M.; Maitra, A.; Allison, J. P.; LeBleu, V. S.; Kalluri, R. Depletion of carcinoma-associated fibroblasts and fibrosis induces immunosuppression and accelerates pancreas cancer with reduced survival. *Cancer Cell* **2014**, *25* (6), 719–34.
- (52) Rhim, A. D.; Oberstein, P. E.; Thomas, D. H.; Mirek, E. T.; Palermo, C. F.; Sastra, S. A.; Dekleva, E. N.; Saunders, T.; Becerra, C. P.; Tattersall, I. W.; Westphalen, C. B.; Kitajewski, J.; Fernandez-Barrena, M. G.; Fernandez-Zapico, M. E.; Iacobuzio-Donahue, C.; Olive, K. P.; Stanger, B. Z. Stromal elements act to restrain, rather than support, pancreatic ductal adenocarcinoma. *Cancer Cell* **2014**, *25* (6), 735–47.
- (53) Anshup; Venkataraman, J. S.; Subramaniam, C.; Kumar, R. R.; Priya, S.; Kumar, T. S.; Omkumar, R.; John, A.; Pradeep, T. Growth of gold nanoparticles in human cells. *Langmuir* **2005**, *21* (25), 11562–11567.
- (54) Shamsaie, A.; Jonczyk, M.; Sturgis, J. D.; Robinson, J. P.; Irudayaraj, J. Intracellularly grown gold nanoparticles as potential surface-enhanced Raman scattering probes. *Journal of biomedical optics* **2007**, *12* (2), No. 020502.
- (55) Liu, Z.; Hu, C.; Li, S.; Zhang, W.; Guo, Z. Rapid intracellular growth of gold nanostructures assisted by functionalized graphene oxide and its application for surface-enhanced Raman spectroscopy. *Analytical chemistry* **2012**, *84* (23), 10338–10344.
- (56) Wang, J.; Zhang, G.; Li, Q.; Jiang, H.; Liu, C.; Amatore, C.; Wang, X. In vivo self-bio-imaging of tumors through in situ biosynthesized fluorescent gold nanoclusters. *Sci. Rep.* **2013**, *3*, No. 1157.
- (57) El-Said, W. A.; Cho, H. Y.; Yea, C. H.; Choi, J. W. Synthesis of metal nanoparticles inside living human cells based on the intracellular formation process. *Advanced materials* **2014**, *26* (6), 910–918.

- (58) Zhao, C.; Du, T.; Rehman, F. U.; Lai, L.; Liu, X.; Jiang, X.; Li, X.; Chen, Y.; Zhang, H.; Sun, Y. Biosynthesized gold nanoclusters and iron complexes as scaffolds for multimodal cancer bioimaging. *Small* **2016**, *12* (45), 6255–6265.
- (59) West, A. L.; Schaublin, N. M.; Griep, M. H.; Maurer-Gardner, E. I.; Cole, D. P.; Fakner, A. M.; Hussain, S. M.; Karna, S. P. In situ synthesis of fluorescent gold nanoclusters by nontumorigenic microglial cells. *ACS Appl. Mater. Interfaces* **2016**, *8* (33), 21221–21227.
- (60) Drescher, D.; Traub, H.; Büchner, T.; Jakubowski, N.; Kneipp, J. Properties of in situ generated gold nanoparticles in the cellular context. *Nanoscale* **2017**, *9* (32), 11647–11656.
- (61) Rehman, F. U.; Du, T.; Shaikh, S.; Jiang, X.; Chen, Y.; Li, X.; Yi, H.; Hui, J.; Chen, B.; Selke, M. Nano in nano: biosynthesized gold and iron nanoclusters cargo neoplastic exosomes for cancer status biomarking. *Nanomedicine: Nanotechnology, Biology and Medicine* **2018**, *14* (8), 2619–2631.
- (62) Singh, A. V.; Jahnke, T.; Kishore, V.; Park, B.-W.; Batuwangala, M.; Bill, J.; Sitti, M. Cancer cells biomineralize ionic gold into nanoparticles-microplates via secreting defense proteins with specific gold-binding peptides. *Acta biomaterialia* **2018**, *71*, 61–71.
- (63) Singh, A. V.; Alapan, Y.; Jahnke, T.; Laux, P.; Luch, A.; Aghakhani, A.; Kharratian, S.; Onbasli, M. C.; Bill, J.; Sitti, M. Seed-mediated synthesis of plasmonic gold nanoribbons using cancer cells for hyperthermia applications. *J. Mater. Chem. B* **2018**, *6* (46), 7573–7581.
- (64) Ozaki, M.; Yoshida, S.; Tsuruoka, T.; Usui, K. Intracellular mineralization of gold nanoparticles using gold ion-binding peptides with cell-penetrating ability. *Chem. Commun.* **2021**, *57* (6), 725–728.
- (65) Schwartz-Duval, A. S.; Konopka, C. J.; Moitra, P.; Daza, E. A.; Srivastava, I.; Johnson, E. V.; Kampert, T. L.; Fayn, S.; Haran, A.; Dobrucki, L. W. Intratumoral generation of photothermal gold nanoparticles through a vectorized biomineralization of ionic gold. *Nat. Commun.* **2020**, *11* (1), 1–18.
- (66) Wang, J.; Zhang, G.; Li, Q.; Jiang, H.; Liu, C.; Amatore, C.; Wang, X. In vivo self-bio-imaging of tumors through in situ biosynthesized fluorescent gold nanoclusters. *Sci. Rep.* **2013**, *3* (1), 1–6.
- (67) Shaikh, S.; Rehman, F. u.; Du, T.; Jiang, H.; Yin, L.; Wang, X.; Chai, R. Real-Time Multimodal Bioimaging of Cancer Cells and Exosomes through Biosynthesized Iridium and Iron Nanoclusters. *ACS Appl. Mater. Interfaces* **2018**, *10* (31), 26056–26063.
- (68) Forestier, J. Rheumatoid arthritis and its treatment by gold salts. *lancet* **1934**, *224* (5795), 646–648.
- (69) Ahmed, S. V.; Sajjan, R. Chrysiasis: a gold “curse”! *Case Reports* **2009**, *2009*, No. bcr0720080417.
- (70) Fowler, W. A note on the occurrence of chrysiasis following treatment by gold salts. *Tubercle* **1934**, *16*, 539–541.
- (71) Benn, H.-P.; von Gaudecker, B.; Czank, M.; Loeffler, H. Crystalline and amorphous gold in chrysiasis. *Archives of dermatological research* **1990**, *282* (3), 172–178.
- (72) Jemal, A.; Siegel, R.; Ward, E.; Murray, T.; Xu, J.; Smigal, C.; Thun, M. J. Cancer statistics, 2006. *CA Cancer J. Clin* **2006**, *56* (2), 106–30.
- (73) Schwartz-Duval, A. S.; Sokolov, K. V. Prospecting Cellular Gold Nanoparticle Biomineralization as a Viable Alternative to Prefabricated Gold Nanoparticles. *Advanced Science* **2022**, *9* (20), No. 2105957.
- (74) Gradiz, R.; Silva, H. C.; Carvalho, L.; Botelho, M. F.; Mota-Pinto, A. MIA PaCa-2 and PANC-1—pancreas ductal adenocarcinoma cell lines with neuroendocrine differentiation and somatostatin receptors. *Sci. Rep.* **2016**, *6* (1), No. 21648.
- (75) De Baaij, J. H.; Hoenderop, J. G.; Bindels, R. J. Magnesium in man: implications for health and disease. *Physiol. Rev.* **2015**, *95*, 1.
- (76) Fujimichi, Y.; Hamada, N. Ionizing irradiation not only inactivates clonogenic potential in primary normal human diploid lens epithelial cells but also stimulates cell proliferation in a subset of this population. *PLoS One* **2014**, *9* (5), No. e98154.
- (77) Suzuki, K.; Kodama, S.; Watanabe, M. Extremely low-dose ionizing radiation causes activation of mitogen-activated protein kinase pathway and enhances proliferation of normal human diploid cells. *Cancer research* **2001**, *61* (14), 5396–5401.
- (78) Wang, Z.; Lv, M.-Y.; Huang, Y.-X. Effects of low-dose X-ray on cell growth, membrane permeability, DNA damage and gene transfer efficiency. *Dose-Response* **2020**, *18* (4), No. 1559325820962615.
- (79) Ivashkevich, A.; Redon, C. E.; Nakamura, A. J.; Martin, R. F.; Martin, O. A. Use of the γ -H2AX assay to monitor DNA damage and repair in translational cancer research. *Cancer letters* **2012**, *327* (1–2), 123–133.
- (80) Reers, M.; Smith, T. W.; Chen, L. B. J-aggregate formation of a carbocyanine as a quantitative fluorescent indicator of membrane potential. *Biochemistry* **1991**, *30* (18), 4480–4486.
- (81) Camilleri-Broët, S.; Vanderwerff, H.; Caldwell, E.; Hockenbery, D. Distinct alterations in mitochondrial mass and function characterize different models of apoptosis. *Experimental cell research* **1998**, *239* (2), 277–292.
- (82) Ying, W. NAD⁺/NADH and NADP⁺/NADPH in cellular functions and cell death: regulation and biological consequences. *Antioxidants & redox signaling* **2008**, *10* (2), 179–206.
- (83) Liu, H.; Liu, Z.; Wang, Y.; Xiao, J.; Liu, X.; Jiang, H.; Wang, X. Intracellular Liquid-Liquid Phase Separation Induces Tunable Anisotropic Nanocrystal Growth for Multidimensional Analysis. *Adv. Funct. Mater.* **2023**, *33*, No. 2302136.
- (84) Schwartz-Duval, A. S.; Wen, R.; Srivastava, I.; Moitra, P.; Pan, D. A Simplistic Single-Step Method for Preparing Biomimetic Nanoparticles from Endogenous Biomaterials. *ACS Appl. Mater. Interfaces* **2021**, *13*, 46464.
- (85) Zhang, Q.; Wang, J.; Meng, Z.; Ling, R.; Ren, H.; Qin, W.; Wu, Z.; Shao, N. Glutathione disulfide as a reducing, capping, and mass-separating agent for the synthesis and enrichment of gold nanoclusters. *Nanomaterials* **2021**, *11* (9), 2258.
- (86) Turkevich, J.; Stevenson, P. C.; Hillier, J. A study of the nucleation and growth processes in the synthesis of colloidal gold. *Discuss. Faraday Soc.* **1951**, *11*, 55–75.
- (87) Pavlova, N. N.; Zhu, J.; Thompson, C. B. The hallmarks of cancer metabolism: Still emerging. *Cell metabolism* **2022**, *34*, 355.
- (88) Peoples, J. N.; Saraf, A.; Ghazal, N.; Pham, T. T.; Kwong, J. Q. Mitochondrial dysfunction and oxidative stress in heart disease. *Experimental & molecular medicine* **2019**, *51* (12), 1–13.
- (89) Baenke, F.; Peck, B.; Miess, H.; Schulze, A. Hooked on fat: the role of lipid synthesis in cancer metabolism and tumour development. *Disease models & mechanisms* **2013**, *6* (6), 1353–1363.
- (90) Lewin, D.; Lewin, K. J. Small intestine. In *Modern surgical pathology*; Elsevier, 2009; pp 719–754.
- (91) Daems, N.; Michiels, C.; Lucas, S.; Baatout, S.; Aerts, A. Gold nanoparticles meet medical radionuclides. *Nuclear Medicine and Biology* **2021**, *100*, 61–90.
- (92) Neuer, A. L.; Gerken, L. R.; Keevend, K.; Gogos, A.; Herrmann, I. K. Uptake, distribution and radio-enhancement effects of gold nanoparticles in tumor microtissues. *Nanoscale Adv.* **2020**, *2* (7), 2992–3001.
- (93) Frantellizzi, V.; Verrina, V.; Raso, C.; Pontico, M.; Petronella, F.; Bertana, V.; Ballesio, A.; Marasso, S.; Miglietta, S.; Rosa, P. 99mTc-labeled keratin gold-nanoparticles in a nephron-like microfluidic chip for photo-thermal therapy applications. *Materials Today Advances* **2022**, *16*, No. 100286.
- (94) Kreyling, W. G.; Abdelmonem, A. M.; Ali, Z.; Alves, F.; Geiser, M.; Haberl, N.; Hartmann, R.; Hirn, S.; De Aberasturi, D. J.; Kantner, K. In vivo integrity of polymer-coated gold nanoparticles. *Nature Nanotechnol.* **2015**, *10* (7), 619–623.
- (95) Spadavecchia, J.; Apchain, E.; Albric, M.; Fontan, E.; Reiche, I. One-Step Synthesis of Collagen Hybrid Gold Nanoparticles and Formation on Egyptian-like Gold-Plated Archaeological Ivory. *Angew. Chem.* **2014**, *126* (32), 8503–8506.
- (96) Wei, G.; Wang, L.; Sun, L.; Song, Y.; Sun, Y.; Guo, C.; Yang, T.; Li, Z. Type I collagen-mediated synthesis and assembly of UV-photoreduced gold nanoparticles and their application in surface-

enhanced Raman scattering. *J. Phys. Chem. C* **2007**, *111* (5), 1976–1982.

(97) Marisca, O. T.; Kantner, K.; Pfeiffer, C.; Zhang, Q.; Pelaz, B.; Leopold, N.; Parak, W. J.; Rejman, J. Comparison of the in vitro uptake and toxicity of collagen-and synthetic polymer-coated gold nanoparticles. *Nanomaterials* **2015**, *5* (3), 1418–1430.

(98) Zhang, X.-D.; Wu, D.; Shen, X.; Liu, P.-X.; Fan, F.-Y.; Fan, S.-J. In vivo renal clearance, biodistribution, toxicity of gold nanoclusters. *Biomaterials* **2012**, *33* (18), 4628–4638.

(99) Chan, L. L.-Y.; Smith, T.; Kumph, K. A.; Kuksin, D.; Kessel, S.; Déry, O.; Cribbes, S.; Lai, N.; Qiu, J. A high-throughput AO/PI-based cell concentration and viability detection method using the Celigo image cytometry. *Cytotechnology* **2016**, *68* (5), 2015–2025.

(100) Shin, H.; Kwak, M.; Lee, T. G.; Lee, J. Y. Quantifying the level of nanoparticle uptake in mammalian cells using flow cytometry. *Nanoscale* **2020**, *12* (29), 15743–15751.

(101) Choi, S. Y.; Yang, N.; Jeon, S. K.; Yoon, T. H. Semi-quantitative estimation of cellular SiO₂ nanoparticles using flow cytometry combined with X-ray fluorescence measurements. *Cytometry Part A* **2014**, *85* (9), 771–780.

(102) Franken, N. A.; Rodermond, H. M.; Stap, J.; Haveman, J.; Van Bree, C. Clonogenic assay of cells in vitro. *Nature protocols* **2006**, *1* (5), 2315–2319.

(103) Herman, J. M.; Wild, A. T.; Wang, H.; Tran, P. T.; Chang, K. J.; Taylor, G. E.; Donehower, R. C.; Pawlik, T. M.; Ziegler, M. A.; Cai, H.; Savage, D. T.; Canto, M. I.; Klapman, J.; Reid, T.; Shah, R. J.; Hoffe, S. E.; Rosemurgy, A.; Wolfgang, C. L.; Laheru, D. A. Randomized phase III multi-institutional study of TNFerade biologic with fluorouracil and radiotherapy for locally advanced pancreatic cancer: final results. *J. Clin Oncol* **2013**, *31* (7), 886–94.

(104) Schwartz-Duval, A. S.; Mackeyev, Y.; Gagea, M.; Krishnan, S.; Sokolov, K. Biogeochemistry concepts in medicine: Radiosensitizing pancreatic cancer through pathology driven biosynthesis of gold nanoparticles. Version 1. *ChemRxiv* 2023; <https://chemrxiv.org/engage/chemrxiv/article-details/64bff234ae3d1a7b0d5386b9> (accessed 2023-12-12).